



Two-dimensional microtwist modeling of topological polarization in hinged Kagome lattices and its experimental validation

Hui Chen ^{a,b}, Shaoyun Wang ^b, Xiaopeng Li ^b, Guoliang Huang ^{b,*}

^a Piezoelectric Device Laboratory, School of Mechanical Engineering and Mechanics, Ningbo University, Ningbo 315211, China

^b Department of Mechanical and Aerospace Engineering, University of Missouri, Columbia, MO 65211, USA



ARTICLE INFO

Keywords:

Microtwist continuum

Zero modes

Parity asymmetry

Polarized behavior

Hinge-based metamaterials

ABSTRACT

Kagome lattices have recently attracted a great attention because of the unique mechanical properties including their topological polarization and localized zero modes at certain edges, which challenge the standard effective continuum theories. The previous study of these systems has been predominantly focused on the ideal Kagome lattice with the spring-mass models. In this study, we stretch this paradigm by exploring the hinged Kagome lattices towards practical application to understand the topological polarization under the framework of the microtwist continuum. The hinges are modeled by ligaments capable of supporting stretching, shear and bending deformations. The microtwist elasticity is then formulated thanks to leading order two-scale asymptotics and its constitutive and balance equations are derived. Performance of the proposed theory is validated by the exact solution for predicting dispersion relations and periodic zero modes. We further demonstrate the effectiveness of this theory through numerical simulations as well as experimental testing. Finally, nonuniform deformation under complex loadings and parity asymmetric surface waves in microtwist media are explored. Our study provides a great potential of using the microtwist medium to design, control and program hinge-based metamaterials.

1. Introduction

Because of the highest structure efficiency per unit weight, mechanical lattices are broadly used in weight-critical applications like aerospace engineering and automobile industry. When the element has poor connectivity, the lattice-based material exhibits a number of zero deformation modes that cost little to no elastic energy (Grima and Evans, 2000; Coulais, 2016; Coulais et al., 2018; Czajkowski et al., 2022). Although disastrous in some scenarios, the presence of zero modes could be beneficial. The use of pentamode materials with five zero modes is the most spectacular application in acoustic cloaking (Milton and Cherkaev, 1995; Kadic et al., 2012; Norris and Shuvalov, 2011; Milton, 2013). In addition, polar materials with one intrinsic zero mode have been successfully suggested in elastic cloaking (Nassar et al., 2018, 2019, 2020b; Zhang et al., 2020; Xu et al., 2020). In those applications, zero modes in the lattice appear with Parity (P)-symmetry, i.e., the solution invariance under the spatial inversion.

As a matter of fact, there are also mechanical lattices with a broken P-symmetry, which means that the solution is variant under the space inversion. Lattice materials with such property are polarized whose zero modes grow in amplitude in a preferential direction and decay

in the opposite direction. Kagome lattices are one of the outstanding examples on topological polarization in isostatic lattices. For example, a regular Kagome lattice exhibits P-symmetry bulk zero modes which maintain uniform amplitude across the whole lattice. However, general geometric distortions of the lattice will make zero modes polarized where the zero modes adopt exponential profiles that decay towards the bulk and re-localize at free boundaries. Kane and Lubensky (2014) characterized the conditions under which the re-localization of zero modes towards the free boundaries of a distorted lattice happens unevenly and favors certain boundaries over their opposites. The resulting P-asymmetric distribution of zero modes in Kagome lattices are topological in nature which can be quantified by a topological polarization vector, so that they are immune to continuous perturbations, small and large, as long as the signs of distortion parameters remain unchanged. The topological polarization leads to the appearance of elastic polarization effects whereby a finite sample appears hard when indented on one side and soft when indented on the opposite side (Rocklin et al., 2017; Bilal et al., 2017). The polarization behavior due to P-asymmetric zero modes cannot be properly captured from the perspective of conventional continuum mechanics and even micropolar theory (Cosserat and Cosserat, 1909). Recently, based on spring-mass models, we formulated

* Corresponding author.

E-mail address: huangg@missouri.edu (G. Huang).

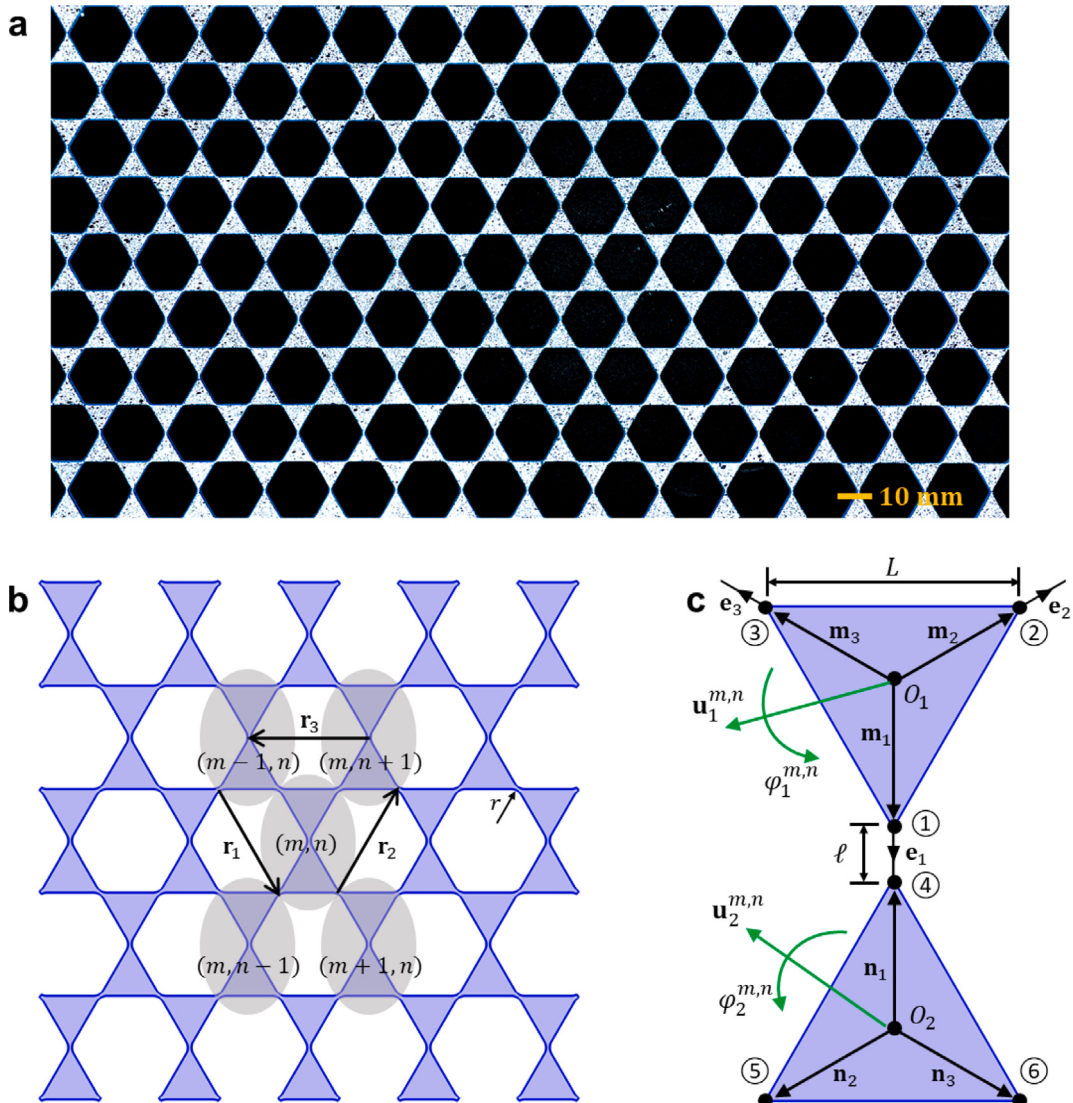


Fig. 1. Discrete modeling of the regular hinged Kagome lattice. (a) Photograph of the regular hinged Kagome lattice. Scale bar, 10 mm. (b) Schematic of the regular hinged Kagome lattice and its corresponding unit cell. (c) The discrete unit cell of the hinged Kagome lattice comprises of rigid equilateral triangles with length L connected by ligaments to support stretching, shear and bending deformations. \mathbf{m}_j and \mathbf{n}_j are the unit vectors from the center “ O_1 ” and “ O_2 ” to nodes (1, 2,3) and nodes (4,5,6), respectively.

a new microtwist theory capable of rendering polarization effects of the ideal 2D Kagome lattice and 3D pyrochlore lattice on a macroscopic scale and quantitatively predicting the polarized indentation response of finite samples (Nassar et al., 2020a; Xia et al., 2021). However, the developed continuum theory cannot directly be applied to study polarization behavior of physical Kagome lattices featuring solid triangles connected with elastic hinges, which can be manufactured via laser cutting technique (see Fig. 1a). The ligaments connecting the triangular plates of each cell are slender beamlike structural elements endowed with finite thickness, which can deform under stretching, shear and bending mechanisms in the plane of the lattice, with the bending stiffness being significantly smaller than the stretching and shear stiffnesses. The local deformation occurring at ligaments, which can be described via three corresponding stiffnesses, has a significant impact on the global characteristics of hinged Kagome lattices. To the best of our knowledge, there exists no known elasticity theory in modeling the hinged Kagome lattices to consider the hybrid mechanism where the hinges carry bending, stretching and shear deformations and quantitatively predict polarization effects.

It is the purpose of the present paper to propose a generalized 2D effective medium theory of the physical hinged Kagome lattice, which

is capable of faithfully reproducing microstructural zero modes and related polarization effects on the continuum scale. Theoretical formulations are conducted for the hinged Kagome lattice by considering the stretching, bending and shear deformations in the ligaments as flexible beams. Specifically, since the bending stiffness of ligaments does not allow free relative rotation of the plates, the zero-energy topological modes are lifted to finite frequencies, which is strikingly different from the one from the ideal Kagome lattices. By progressively perturbing the geometry of regular hinged Kagome lattices so as to transform them into distorted ones, the total displacement field is composed of the macroscopic displacement field and of an additional degree of freedom (DOF), namely the twisting motion, directly related to a microstructural zero mode. The resulting microtwist theory is therefore an enriched continuum allowing for the presence of periodic zero mode in the form of an additional DOF and the additional odd-order tensor elasticity constants are responsible for non-standard elasticity behavior, in particular P-asymmetry.

The paper is organized as follows. In Section 2, we establish a discrete model by replacing hinges with flexible beams and determine the governing equations. Periodic zero modes in hinged Kagome lattices are then investigated. In Section 3, we take the perturbation assumptions and derive microtwist elasticity for the weakly-distorted hinged

Kagome lattices. The performance of microtwist elasticity is then validated by comparing with the exact solution of dispersion relations and zero modes for hinged Kagome lattices. In Section 4, we validate the microtwist theory through indentation and three-point bending experiments. In Section 5, we provide numerical demonstrations of nonuniform deformations and parity asymmetric wave behaviors in microtwist media. The last section contains a brief conclusion.

2. Kinematics and dynamics of the hinged Kagome lattices and zero modes

General hinged Kagome lattices are introduced and classified into two phases, regular and distorted, based on the number and type of zero modes they support. To capture the zero modes of the hinged Kagome lattices, we first establish a discrete model in which we consider rigid triangles connected by ligaments acting as hinges which are represented by flexible beams with finite length to support stretching, shear and bending deformations. Their geometry, kinematics and dynamics of the lattices are then formulated in anticipation of the needs of formulation of the microtwist theory in Section 3.

2.1. Discrete modeling of the hinged Kagome lattices

Consider the regular hinged Kagome lattice shown in Fig. 1b in a periodic reference configuration. The lattice are composed of a network of solid triangles connected by thin ligaments. Vectors $\mathbf{r}_j, j \in \{1, 2, 3\}$ are lattice vectors: the reference configuration is invariant by translation along any integer linear combination of the \mathbf{r}_j (see Appendix A). The unit cell of the hinged Kagome lattice is modeled as shown in Fig. 1c, which is composed of two solid triangles connecting with the ligament with a finite length ℓ and six nodes on their vertices with the basis $\mathbf{x}_k, k \in \{1, 2, 3, 4, 5, 6\}$. The ligaments are deformed as elastic beams to admit stretching, shear and bending deformations, with stiffnesses being k_l , k_s and k_b , respectively. In order to capture the ligament deformation, the three elastic stiffnesses are independently determined by applying three small patterned deformations for a specific hinge geometry (details in Appendix B). It is also noted that the stored elastic energy due to bending deformation in the ligament is much smaller than those due to stretching and shear deformations. The initial position of node k in unit cell (m, n) reads

$$\mathbf{x}_k^{m,n} = \mathbf{x}_k + \mathbf{x}'^{m,n}, \quad \mathbf{x}^{m,n} = m\mathbf{r}_1 + n\mathbf{r}_2, \quad (m, n) \in \mathbb{Z}^2. \quad (1)$$

Each unit cell (m, n) has six degrees of freedom: the translation displacements, $\mathbf{u}_i^{m,n}$, and the rotational motions $\varphi_i^{m,n}$ with $i \in \{1, 2\}$. We let the origin of coordinates “ O_1 ” and “ O_2 ” be the geometric center of the two triangles, respectively. Accordingly, the reference positions of nodes 1, 2 and 3 in the top triangle, with respect to the origin “ O_1 ”, are

$$\mathbf{x}_1 = a\mathbf{m}_1, \quad \mathbf{x}_2 = a\mathbf{m}_2, \quad \mathbf{x}_3 = a\mathbf{m}_3, \quad (2)$$

and the reference positions of nodes 4, 5 and 6 in the bottom triangle, with respect to the origin “ O_2 ”, are

$$\mathbf{x}_4 = a\mathbf{n}_1, \quad \mathbf{x}_5 = a\mathbf{n}_2, \quad \mathbf{x}_6 = a\mathbf{n}_3, \quad (3)$$

with a denoting the length between nodes and the corresponding origins. The corresponding unit vectors of flexible beams can be obtained as

$$\mathbf{e}_j = \frac{\mathbf{m}_j - \mathbf{n}_j}{\|\mathbf{m}_j - \mathbf{n}_j\|}. \quad (4)$$

There exist three independent deformations in the ligament. The stretching deformation can be obtained as

$$\begin{aligned} \Delta_{l_1}^{m,n} &= \langle \mathbf{e}_1, (\mathbf{u}_2^{m,n} + a\bar{\mathbf{n}}_1\varphi_2^{m,n}) - (\mathbf{u}_1^{m,n} + a\bar{\mathbf{m}}_1\varphi_1^{m,n}) \rangle, \\ \Delta_{l_2}^{m,n} &= \langle \mathbf{e}_2, (\mathbf{u}_2^{m,n+1} + a\bar{\mathbf{n}}_2\varphi_2^{m,n+1}) - (\mathbf{u}_1^{m,n} + a\bar{\mathbf{m}}_2\varphi_1^{m,n}) \rangle, \\ \Delta_{l_3}^{m,n} &= \langle \mathbf{e}_3, (\mathbf{u}_2^{m-1,n} + a\bar{\mathbf{n}}_3\varphi_2^{m-1,n}) - (\mathbf{u}_1^{m,n} + a\bar{\mathbf{m}}_3\varphi_1^{m,n}) \rangle, \end{aligned} \quad (5)$$

and the shear deformation is

$$\begin{aligned} \Delta_{s_1}^{m,n} &= \langle \bar{\mathbf{e}}_1, (\mathbf{u}_2^{m,n} + a\bar{\mathbf{n}}_1\varphi_2^{m,n}) - (\mathbf{u}_1^{m,n} + a\bar{\mathbf{m}}_1\varphi_1^{m,n}) \rangle - \ell(\varphi_1^{m,n} + \varphi_2^{m,n})/2, \\ \Delta_{s_2}^{m,n} &= \langle \bar{\mathbf{e}}_2, (\mathbf{u}_2^{m,n+1} + a\bar{\mathbf{n}}_2\varphi_2^{m,n+1}) - (\mathbf{u}_1^{m,n} + a\bar{\mathbf{m}}_2\varphi_1^{m,n}) \rangle - \ell(\varphi_1^{m,n} + \varphi_2^{m,n+1})/2, \\ \Delta_{s_3}^{m,n} &= \langle \bar{\mathbf{e}}_3, (\mathbf{u}_2^{m-1,n} + a\bar{\mathbf{n}}_3\varphi_2^{m-1,n}) - (\mathbf{u}_1^{m,n} + a\bar{\mathbf{m}}_3\varphi_1^{m,n}) \rangle - \ell(\varphi_1^{m,n} + \varphi_2^{m-1,n})/2, \end{aligned} \quad (6)$$

and the bending deformation is

$$\begin{aligned} \Delta_{\theta_1}^{m,n} &= \varphi_2^{m,n} - \varphi_1^{m,n}, \\ \Delta_{\theta_2}^{m,n} &= \varphi_2^{m,n+1} - \varphi_1^{m,n}, \\ \Delta_{\theta_3}^{m,n} &= \varphi_2^{m-1,n} - \varphi_1^{m,n}, \end{aligned} \quad (7)$$

where $\langle \cdot \rangle$ is the inner product and a superimposed bar symbolizes a plane rotation of $\pi/2$.

Then, the forces acting at the center of two triangles can be written as

$$\begin{aligned} \mathbf{F}_1^{m,n} &= k_l(\Delta_{l_1}^{m,n}\mathbf{e}_1 + \Delta_{l_2}^{m,n}\mathbf{e}_2 + \Delta_{l_3}^{m,n}\mathbf{e}_3) + k_s(\Delta_{s_1}^{m,n}\bar{\mathbf{e}}_1 + \Delta_{s_2}^{m,n}\bar{\mathbf{e}}_2 + \Delta_{s_3}^{m,n}\bar{\mathbf{e}}_3) \\ &\quad + k_b(\Delta_{\theta_1}^{m,n}\bar{\mathbf{m}}_1/a + \Delta_{\theta_2}^{m,n}\bar{\mathbf{m}}_2/a + \Delta_{\theta_3}^{m,n}\bar{\mathbf{m}}_3/a), \end{aligned} \quad (8)$$

and

$$\begin{aligned} \mathbf{F}_2^{m,n} &= -k_l(\Delta_{l_1}^{m,n}\mathbf{e}_1 + \Delta_{l_2}^{m,n-1}\mathbf{e}_2 + \Delta_{l_3}^{m+1,n}\mathbf{e}_3) - k_s(\Delta_{s_1}^{m,n}\bar{\mathbf{e}}_1 + \Delta_{s_2}^{m,n}\bar{\mathbf{e}}_2 \\ &\quad + \Delta_{s_3}^{m,n}\bar{\mathbf{e}}_3) - k_b(\Delta_{\theta_1}^{m,n}\bar{\mathbf{n}}_1/a + \Delta_{\theta_2}^{m,n-1}\bar{\mathbf{n}}_2/a + \Delta_{\theta_3}^{m+1,n}\bar{\mathbf{n}}_3/a). \end{aligned} \quad (9)$$

The moments acting at the center of two triangles can be obtained as

$$\begin{aligned} M_1^{m,n} &= k_l(\Delta_{l_1}^{m,n}\langle \mathbf{e}_1, a\bar{\mathbf{m}}_1 \rangle + \Delta_{l_2}^{m,n}\langle \mathbf{e}_2, a\bar{\mathbf{m}}_2 \rangle + \Delta_{l_3}^{m,n}\langle \mathbf{e}_3, a\bar{\mathbf{m}}_3 \rangle) \\ &\quad + k_s(\Delta_{s_1}^{m,n}\langle \bar{\mathbf{e}}_1, a\bar{\mathbf{m}}_1 \rangle + \Delta_{s_2}^{m,n}\langle \bar{\mathbf{e}}_2, a\bar{\mathbf{m}}_2 \rangle + \Delta_{s_3}^{m,n}\langle \bar{\mathbf{e}}_3, a\bar{\mathbf{m}}_3 \rangle) \\ &\quad + k_b(\Delta_{\theta_1}^{m,n} + \Delta_{\theta_2}^{m,n} + \Delta_{\theta_3}^{m,n}), \end{aligned} \quad (10)$$

and

$$\begin{aligned} M_2^{m,n} &= -k_l(\Delta_{l_1}^{m,n}\langle \mathbf{e}_1, a\bar{\mathbf{n}}_1 \rangle + \Delta_{l_2}^{m,n-1}\langle \mathbf{e}_2, a\bar{\mathbf{n}}_2 \rangle + \Delta_{l_3}^{m+1,n}\langle \mathbf{e}_3, a\bar{\mathbf{n}}_3 \rangle) \\ &\quad - k_s(\Delta_{s_1}^{m,n}\langle \bar{\mathbf{e}}_1, a\bar{\mathbf{n}}_1 \rangle + \Delta_{s_2}^{m,n-1}\langle \bar{\mathbf{e}}_2, a\bar{\mathbf{n}}_2 \rangle + \Delta_{s_3}^{m+1,n}\langle \bar{\mathbf{e}}_3, a\bar{\mathbf{n}}_3 \rangle) \\ &\quad - k_b(\Delta_{\theta_1}^{m,n} + \Delta_{\theta_2}^{m,n-1} + \Delta_{\theta_3}^{m+1,n}). \end{aligned} \quad (11)$$

Finally, the equations of the motion of the unit cell (m, n) can be stated as

$$\begin{aligned} m_i \ddot{\mathbf{u}}_i^{m,n} &= \mathbf{F}_i^{m,n}, \\ I_i \ddot{\varphi}_i^{m,n} &= M_i^{m,n}, \end{aligned} \quad (12)$$

where m_i and I_i are the mass and moment of inertia of the i th triangle, respectively, with

$$\begin{aligned} I_1 &= \frac{m_1}{36}(\|\mathbf{am}_2 - \mathbf{am}_3\|^2 + \|\mathbf{am}_3 - \mathbf{am}_1\|^2 + \|\mathbf{am}_1 - \mathbf{am}_2\|^2), \\ I_2 &= \frac{m_2}{36}(\|\mathbf{an}_2 - \mathbf{an}_3\|^2 + \|\mathbf{an}_3 - \mathbf{an}_1\|^2 + \|\mathbf{an}_1 - \mathbf{an}_2\|^2). \end{aligned}$$

2.2. Periodic zero modes

Analyzing configurations where the various fields of interest vary slowly with respect to time and the unit cell index (m, n) is key to building an effective substitution medium of hinged Kagome lattices. By the same logic, the configurations of the unit cell do not depend on time and (m, n) either. These are referred to static periodic configurations and are adopted in the remained of this section for the purpose of the theory of microtwist homogenization presented in Section 3.

Dismissing the dependence over (m, n) greatly simplifies the equations in Section 2.1. As a result, stretching and shear deformations are given by the matrix product

$$\begin{bmatrix} \Delta_{l_1} \\ \Delta_{l_2} \\ \Delta_{l_3} \\ \Delta_{s_1} \\ \Delta_{s_2} \\ \Delta_{s_3} \end{bmatrix} = (\mathbf{C}_l + \mathbf{C}_\ell) \begin{bmatrix} \mathbf{u}_1 \\ \mathbf{u}_2 \\ \varphi_1 \\ \varphi_2 \end{bmatrix}, \quad (13)$$

where

$$\mathbf{C}_l = \begin{bmatrix} -\mathbf{e}'_1 & \mathbf{e}'_1 & -\langle \mathbf{e}_1, a\bar{\mathbf{n}}_1 \rangle & \langle \mathbf{e}_1, a\bar{\mathbf{n}}_1 \rangle \\ -\mathbf{e}'_2 & \mathbf{e}'_2 & -\langle \mathbf{e}_2, a\bar{\mathbf{n}}_2 \rangle & \langle \mathbf{e}_2, a\bar{\mathbf{n}}_2 \rangle \\ -\mathbf{e}'_3 & \mathbf{e}'_3 & -\langle \mathbf{e}_3, a\bar{\mathbf{n}}_3 \rangle & \langle \mathbf{e}_3, a\bar{\mathbf{n}}_3 \rangle \\ -\bar{\mathbf{e}}'_1 & \bar{\mathbf{e}}'_1 & -\langle \bar{\mathbf{e}}_1, a\bar{\mathbf{n}}_1 \rangle & \langle \bar{\mathbf{e}}_1, a\bar{\mathbf{n}}_1 \rangle \\ -\bar{\mathbf{e}}'_2 & \bar{\mathbf{e}}'_2 & -\langle \bar{\mathbf{e}}_2, a\bar{\mathbf{n}}_2 \rangle & \langle \bar{\mathbf{e}}_2, a\bar{\mathbf{n}}_2 \rangle \\ -\bar{\mathbf{e}}'_3 & \bar{\mathbf{e}}'_3 & -\langle \bar{\mathbf{e}}_3, a\bar{\mathbf{n}}_3 \rangle & \langle \bar{\mathbf{e}}_3, a\bar{\mathbf{n}}_3 \rangle \end{bmatrix}, \quad (14)$$

$$\mathbf{C}_\ell = \begin{bmatrix} 0 & 0 & 0 & 0 \\ 0 & 0 & 0 & 0 \\ 0 & 0 & 0 & 0 \\ 0 & 0 & -\ell/2 & -\ell/2 \\ 0 & 0 & -\ell/2 & -\ell/2 \\ 0 & 0 & -\ell/2 & -\ell/2 \end{bmatrix},$$

with a prime being a conjugate transpose. Meanwhile, the bending deformation is given by the following matrix product:

$$\begin{bmatrix} 0 \\ 0 \\ 0 \\ \Delta_{\theta_1} \\ \Delta_{\theta_2} \\ \Delta_{\theta_3} \end{bmatrix} = \mathbf{C}_b \begin{bmatrix} \mathbf{u}_1 \\ \mathbf{u}_2 \\ \varphi_1 \\ \varphi_2 \end{bmatrix}, \quad \mathbf{C}_b = \begin{bmatrix} 0 & 0 & 0 & 0 \\ 0 & 0 & 0 & 0 \\ 0 & 0 & 0 & 0 \\ 0 & 0 & -1 & 1 \\ 0 & 0 & -1 & 1 \\ 0 & 0 & -1 & 1 \end{bmatrix}. \quad (15)$$

Then, forces and moments in the unit cell can be expressed as

$$\begin{bmatrix} \mathbf{F}_1 \\ \mathbf{F}_2 \\ \mathbf{M}_1 \\ \mathbf{M}_2 \end{bmatrix} = -\mathbf{C}'_l \mathbf{K} \begin{bmatrix} \Delta_{l_1} \\ \Delta_{l_2} \\ \Delta_{l_3} \\ \Delta_{s_1} \\ \Delta_{s_2} \\ \Delta_{s_3} \end{bmatrix} - \mathbf{E}_b \mathbf{K}_b \begin{bmatrix} 0 \\ 0 \\ 0 \\ \Delta_{\theta_1} \\ \Delta_{\theta_2} \\ \Delta_{\theta_3} \end{bmatrix}, \quad (16)$$

$$\mathbf{E}_b = \begin{bmatrix} 0 & 0 & 0 & -\bar{\mathbf{m}}_1/a & -\bar{\mathbf{m}}_2/a & -\bar{\mathbf{m}}_3/a \\ 0 & 0 & 0 & \bar{\mathbf{n}}_1/a & \bar{\mathbf{n}}_2/a & \bar{\mathbf{n}}_3/a \\ 0 & 0 & 0 & -1 & -1 & -1 \\ 0 & 0 & 0 & 1 & 1 & 1 \end{bmatrix},$$

where $\mathbf{K} = \text{diag}(k_l, k_l, k_l, k_s, k_s, k_s)$ and $\mathbf{K}_b = \text{diag}(0, 0, 0, k_b, k_b, k_b)$ are diagonal matrices gathering the elastic constants of the beam. Accordingly, the equation of motion for periodic configurations of the hinged Kagome lattice can be expressed as

$$-\left[\mathbf{C}'_l \mathbf{K} (\mathbf{C}_l + \mathbf{C}_\ell) + \mathbf{E}_b \mathbf{K}_b \mathbf{C}_b \right] \Phi + \mathbf{F} = \mathbf{G} \ddot{\Phi}, \quad \Phi = \begin{bmatrix} \mathbf{u}_1 \\ \mathbf{u}_2 \\ \varphi_1 \\ \varphi_2 \end{bmatrix}, \quad (17)$$

with $\mathbf{G} = \text{diag}(m_1 \mathbf{I}, m_2 \mathbf{I}, I_1, I_2)$ being the mass matrix, \mathbf{I} being the 2×2 identity matrix and \mathbf{F} being a column $(\mathbf{f}_1, \mathbf{f}_2, \tau_1, \tau_2)$ of external forces periodically applied to the center of two triangles. At last, dismissing dependence upon time yields the equilibrium equation for static periodic configurations:

$$-\left[\mathbf{C}'_l \mathbf{K} (\mathbf{C}_l + \mathbf{C}_\ell) + \mathbf{E}_b \mathbf{K}_b \mathbf{C}_b \right] \Phi + \mathbf{F} = \mathbf{0}. \quad (18)$$

We then refer to Φ as a periodic zero mode when it is a free solution of the above equation (18), i.e., under $\mathbf{F} = 0$. A periodic zero mode necessarily stores zero elastic energy as

$$\sum_j k_l \Delta_{l_j}^2 + k_s \Delta_{s_j}^2 + k_b \Delta_{\theta_j}^2 = 0, \quad j \in \{1, 2, 3\}. \quad (19)$$

In the hinged lattice, $k_b \Delta_{\theta_j}^2 \ll \min\{k_l \Delta_{l_j}^2, k_s \Delta_{s_j}^2\}$ (see Appendix B). As such, a zero mode is a configuration of the lattice where no deformations are due to stretching and shear so that

$$\Delta_{l_j} = \Delta_{s_j} = 0. \quad (20)$$

Specifically, deformations due to the stretching and shear are given by

$$\Delta = \begin{bmatrix} \Delta_{l_1} \\ \Delta_{l_2} \\ \Delta_{l_3} \\ \Delta_{s_1} \\ \Delta_{s_2} \\ \Delta_{s_3} \end{bmatrix} = \mathbf{C} \begin{bmatrix} \mathbf{u}_1 \\ \mathbf{u}_2 \\ \varphi_1 \\ \varphi_2 \end{bmatrix}, \quad (21)$$

where \mathbf{C} is the compatibility matrix and takes the matrix form

$$\mathbf{C} = \begin{bmatrix} -\mathbf{e}'_1 & \mathbf{e}'_1 & -\langle \mathbf{e}_1, a\bar{\mathbf{n}}_1 \rangle & \langle \mathbf{e}_1, a\bar{\mathbf{n}}_1 \rangle \\ -\mathbf{e}'_2 & \mathbf{e}'_2 & -\langle \mathbf{e}_2, a\bar{\mathbf{n}}_2 \rangle & \langle \mathbf{e}_2, a\bar{\mathbf{n}}_2 \rangle \\ -\mathbf{e}'_3 & \mathbf{e}'_3 & -\langle \mathbf{e}_3, a\bar{\mathbf{n}}_3 \rangle & \langle \mathbf{e}_3, a\bar{\mathbf{n}}_3 \rangle \\ -\bar{\mathbf{e}}'_1 & \bar{\mathbf{e}}'_1 & -\langle \bar{\mathbf{e}}_1, a\bar{\mathbf{n}}_1 \rangle - \ell/2 & \langle \bar{\mathbf{e}}_1, a\bar{\mathbf{n}}_1 \rangle - \ell/2 \\ -\bar{\mathbf{e}}'_2 & \bar{\mathbf{e}}'_2 & -\langle \bar{\mathbf{e}}_2, a\bar{\mathbf{n}}_2 \rangle - \ell/2 & \langle \bar{\mathbf{e}}_2, a\bar{\mathbf{n}}_2 \rangle - \ell/2 \\ -\bar{\mathbf{e}}'_3 & \bar{\mathbf{e}}'_3 & -\langle \bar{\mathbf{e}}_3, a\bar{\mathbf{n}}_3 \rangle - \ell/2 & \langle \bar{\mathbf{e}}_3, a\bar{\mathbf{n}}_3 \rangle - \ell/2 \end{bmatrix}. \quad (22)$$

Then, periodic zero modes are null vectors of matrix \mathbf{C} . By the rank-nullity theorem, their number is equal to $Z = 6 - \text{rank } \mathbf{C}$ where 6 is the dimension of \mathbf{C} and $\text{rank } \mathbf{C}$ its rank. On the other hand, the first three lines of matrix \mathbf{C} are necessarily linearly independent, so that $\text{rank } \mathbf{C} \geq 3$ leaves us with two possibilities: $(Z, \text{rank } \mathbf{C}) = (2, 4)$ or $(3, 3)$. Lattices satisfying $Z = 2$ are the ones we call distorted. These have no zero modes other than translations and have initially at least one pair $(\mathbf{m}_j, \mathbf{n}_j)$ of misaligned edges. Hinged Kagome lattices that do not belong to this first class will be called regular. These satisfy $Z = 3$ and have initially aligned edges: $\mathbf{m}_j = -\mathbf{n}_j$. Therefore, the compatibility matrix \mathbf{C} of a regular lattice can be further simplified as

$$\mathbf{C}_0 = \mathbf{C}_{l0} + \mathbf{C}_{\ell0} = \begin{bmatrix} -\mathbf{e}'_1 & \mathbf{e}'_1 & 0 & 0 \\ -\mathbf{e}'_2 & \mathbf{e}'_2 & 0 & 0 \\ -\mathbf{e}'_3 & \mathbf{e}'_3 & 0 & 0 \\ -\bar{\mathbf{e}}'_1 & \bar{\mathbf{e}}'_1 & -a - \ell/2 & -a - \ell/2 \\ -\bar{\mathbf{e}}'_2 & \bar{\mathbf{e}}'_2 & -a - \ell/2 & -a - \ell/2 \\ -\bar{\mathbf{e}}'_3 & \bar{\mathbf{e}}'_3 & -a - \ell/2 & -a - \ell/2 \end{bmatrix}. \quad (23)$$

Global translations are characterized by $\mathbf{u}_1 = \mathbf{u}_2 = \mathbf{U}$ and take the matrix form as

$$\Phi_0 = \mathbf{D}\mathbf{U}, \quad \mathbf{D} = \begin{bmatrix} \mathbf{I} \\ \mathbf{I} \\ \mathbf{0} \\ \mathbf{0} \end{bmatrix}, \quad (24)$$

which clearly satisfy $\mathbf{C}_0 \Phi_0 = \mathbf{0}$. In addition to two periodic translation zero modes, the lattice also admits a third one given by the twist motion between two triangles

$$\Phi_0 = \mathbf{T}\varphi, \quad \mathbf{T} = \begin{bmatrix} 0 \\ 0 \\ -1 \\ 1 \end{bmatrix}. \quad (25)$$

Consequently, the periodic zero modes of a regular hinged Kagome lattice are given by the linear combination

$$\Phi_0 = \mathbf{D}\mathbf{U} + \mathbf{T}\varphi. \quad (26)$$

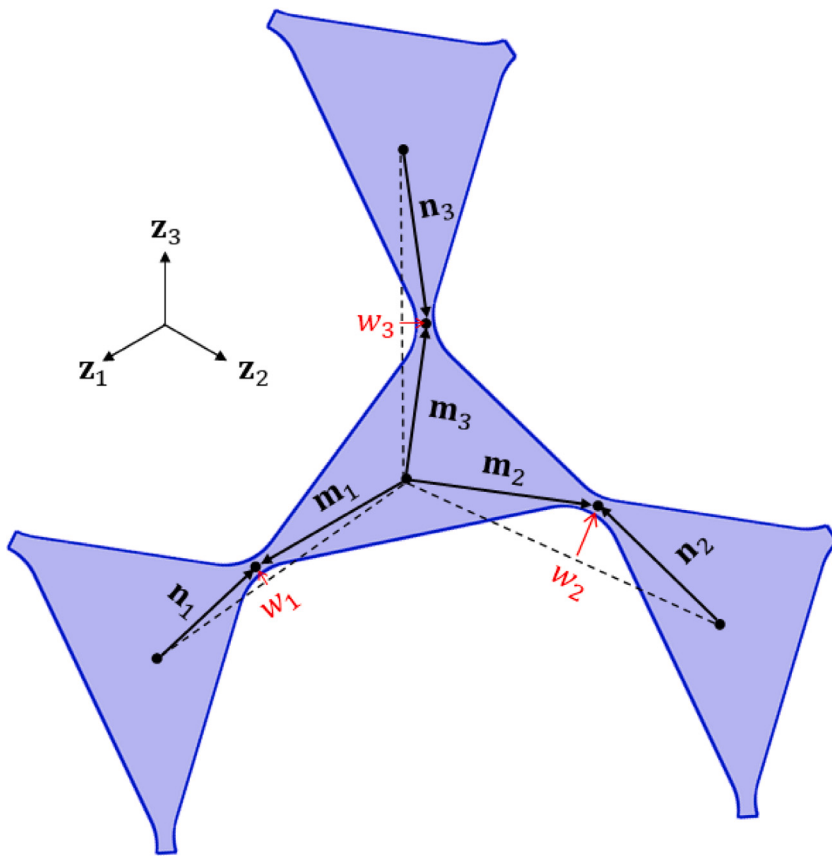


Fig. 2. Illustration of distortion parameters w_j (red arrows) inducing a regular-distorted phase transition from the hinged regular Kagome lattice to the hinged distorted Kagome lattice. The elevations w_j are the only components of the distortion that are relevant here.

3. Microtwist modeling of weakly-distorted hinged Kagome lattices

3.1. Perturbation assumptions

Having fully characterized the static periodic configurations of hinged Kagome lattices in their default regular state, it is time to capture the polarized mechanical behavior of distorted hinged Kagome lattices by introducing four perturbations. Starting with a regular hinged Kagome lattice, a phase transition can be induced by finitely perturbing the initial positions of the nodes so as to break the alignment of any one of the three pairs $(\mathbf{m}_j, \mathbf{n}_j)$; see Fig. 2. Letting $(\mathbf{z}_j, \bar{\mathbf{z}}_j)$ be an orthonormal basis where \mathbf{z}_j is parallel to $a(\mathbf{m}_j - \mathbf{n}_j)$, a weakly-distorted lattice is characterized by

$$\mathbf{m}_j = \mathbf{z}_j + \frac{w_j}{a} \bar{\mathbf{z}}_j + O\left(\frac{w_j}{a}\right)^2, \quad \mathbf{n}_j = -\mathbf{z}_j + \frac{w_j}{a} \bar{\mathbf{z}}_j + O\left(\frac{w_j}{a}\right)^2, \quad |w_j| \ll a. \quad (27)$$

Second, we assume that the translational and rotational displacements $\mathbf{u}_i^{m,n}$ and $\varphi_i^{m,n}$ derive from slowly varying smooth functions $\mathbf{u}_i(\mathbf{x})$ and $\varphi_i(\mathbf{x})$ upon replacing \mathbf{x} with $\mathbf{x}^{m,n}$, where the position variable \mathbf{x} is identified as a slow variable attached to the structure, while \mathbf{u}_i and φ_i are fast scale variables attached to the unit cell in the long wavelength limit, such as wavenumber $\mathbf{q} \rightarrow \mathbf{0}$. Then, the relevant field variables are approximated by the leading-order Taylor expansions

$$\begin{aligned} \mathbf{u}_i^{m+1,n} - \mathbf{u}_i^{m,n} &= \partial_1 \mathbf{u}_i, \\ \mathbf{u}_i^{m,n+1} - \mathbf{u}_i^{m,n} &= \partial_2 \mathbf{u}_i, \\ \varphi_i^{m+1,n} - \varphi_i^{m,n} &= \partial_1 \varphi_i, \\ \varphi_i^{m,n+1} - \varphi_i^{m,n} &= \partial_2 \varphi_i, \end{aligned} \quad (28)$$

where $\partial_i = \langle \mathbf{r}_i, \Delta \rangle$ is the differential with respect to \mathbf{x} in direction \mathbf{r}_i . Then, the functions \mathbf{u}_i and φ_i are slowly varying in space if and only if $\|\partial_i\| \ll 1$.

Third, we assume that the translational and rotational displacements $\mathbf{u}_i^{m,n}$ and $\varphi_i^{m,n}$ are no longer necessarily static but can change with respect to time at small angular frequency ω satisfying $\omega \ll \sqrt{\min(k_s, k_l)/\max(m_i, I_i)}$.

At last, bending stiffness k_b is much smaller than $k_s a^2$ and $k_s a^2$ so that it can be understood as a second-order quantity (see Appendix B).

3.2. Asymptotic expansions

The compatibility relations are given by

$$\mathbf{C} = \mathbf{C}_l + \mathbf{C}_\ell = \mathbf{C}_0 + \delta \mathbf{C}, \quad (29)$$

where \mathbf{C} is the compatibility operator, \mathbf{C}_0 is its restriction to periodic configurations over a regular lattice, and $\delta \mathbf{C}$ is its first-order correction. \mathbf{C}_0 is given by

$$\mathbf{C}_0 = \mathbf{C}_{l0} + \mathbf{C}_{\ell0} = \begin{bmatrix} -\mathbf{z}'_1 & \mathbf{z}'_1 & 0 & 0 \\ -\mathbf{z}'_2 & \mathbf{z}'_2 & 0 & 0 \\ -\mathbf{z}'_3 & \mathbf{z}'_3 & 0 & 0 \\ -\bar{\mathbf{z}}'_1 & \bar{\mathbf{z}}'_1 & -a - \ell/2 & -a - \ell/2 \\ -\bar{\mathbf{z}}'_2 & \bar{\mathbf{z}}'_2 & -a - \ell/2 & -a - \ell/2 \\ -\bar{\mathbf{z}}'_3 & \bar{\mathbf{z}}'_3 & -a - \ell/2 & -a - \ell/2 \end{bmatrix}. \quad (30)$$

The correction $\delta \mathbf{C}$ is composed of three terms $\delta \mathbf{C} = \delta_u \mathbf{C} + \delta_x \mathbf{C} + \delta_\ell \mathbf{C}$, the first of which is due to the perturbation that induces the

regular-distorted phase transition:

$$\delta_w \mathbf{C} = \begin{bmatrix} 0 & 0 & w_1 & -w_1 \\ 0 & 0 & w_2 & -w_2 \\ 0 & 0 & w_3 & -w_3 \\ 0 & 0 & 0 & 0 \\ 0 & 0 & 0 & 0 \\ 0 & 0 & 0 & 0 \end{bmatrix}, \quad (31)$$

and the last two of which are due to the fields being slowly varying in space:

$$\delta_x \mathbf{C} = \begin{bmatrix} 0 & 0 & 0 & 0 \\ 0 & \mathbf{z}'_2 \partial_2 & 0 & 0 \\ 0 & -\mathbf{z}'_3 \partial_1 & 0 & 0 \\ 0 & 0 & 0 & 0 \\ 0 & \bar{\mathbf{z}}'_2 \partial_2 & 0 & -a \partial_2 \\ 0 & -\bar{\mathbf{z}}'_3 \partial_1 & 0 & a \partial_1 \end{bmatrix}, \quad (32)$$

and

$$\delta_\ell \mathbf{C} = \begin{bmatrix} 0 & 0 & 0 & 0 \\ 0 & 0 & 0 & 0 \\ 0 & 0 & 0 & 0 \\ 0 & 0 & 0 & 0 \\ 0 & 0 & 0 & -\ell \partial_2 / 2 \\ 0 & 0 & 0 & \ell \partial_1 / 2 \end{bmatrix}. \quad (33)$$

The motion equation then reads

$$-\mathbf{C}'_l \mathbf{K} \Phi - \mathbf{E}_b \mathbf{K}_b \mathbf{C}_b \Phi + \mathbf{F} = -\omega^2 \mathbf{G} \Phi, \quad (34)$$

where $\mathbf{K} = \text{diag}(k_l, k_l, k_l, k_s, k_s, k_s)$ and $\mathbf{G} = \text{diag}(m_1 \mathbf{I}, m_2 \mathbf{I}, I_1, I_2)$. It is worth mentioning that \mathbf{F} in Eq. (34) correspond to body force and momentum and are taken to be slowly varying in space and of second-order quantities. Displacements Φ can also be Taylor-expanded as

$$\Phi = \Phi_0 + \delta\Phi + \delta^2\Phi + \dots, \quad (35)$$

where Φ_0 gathers the leading-order displacements, $\delta\Phi$ their first-order corrections and so on. In the following, we derive an equation that governs the leading-order displacements Φ_0 thus interpreted as the macroscopic motion equation of the hinged Kagome lattice. In order to accomplish that, Eq. (34) will be solved to leading and first orders.

3.3. Leading and first order displacements

Keeping only leading-order terms in the motion equation (34) yields

$$-\mathbf{C}'_{l0} \mathbf{K} \mathbf{C}_0 \Phi_0 = \mathbf{0}. \quad (36)$$

The solutions to this equation are periodic zero modes so that there exists a vector \mathbf{U} and an angle φ such that

$$\Phi_0 = \mathbf{D}\mathbf{U} + \mathbf{T}\varphi. \quad (37)$$

Keeping the first-order terms in the motion equation (34) yields

$$-\mathbf{C}'_{l0} \mathbf{K} \mathbf{C}_0 \delta\Phi - (\delta_w \mathbf{C} + \delta_x \mathbf{C}) \mathbf{K} \mathbf{C}_0 \Phi_0 - \mathbf{C}'_{l0} \mathbf{K} (\delta_w \mathbf{C} + \delta_x \mathbf{C} + \delta_\ell \mathbf{C}) \Phi_0 = \mathbf{0}. \quad (38)$$

Therein, the term $(\delta_w \mathbf{C} + \delta_x \mathbf{C}) \mathbf{K} \mathbf{C}_0 \Phi_0$ vanishes as $\mathbf{C}_0 \Phi_0 = \mathbf{0}$. The above equation (38) then can be simplified as

$$-\mathbf{C}'_{l0} \mathbf{K} \mathbf{C}_0 \delta\Phi + \Psi = \mathbf{0}, \quad \Psi = -\mathbf{C}'_{l0} \mathbf{K} (\delta_w \mathbf{C} + \delta_x \mathbf{C} + \delta_\ell \mathbf{C}) \Phi_0. \quad (39)$$

Here matrix \mathbf{C}_{l0} being singular, the above equation (39) admits solutions if and only if Ψ is balanced in the sense of being orthogonal to all periodic zero modes

$$\mathbf{D}' \Psi = \mathbf{0}, \quad \mathbf{T}' \Psi = \mathbf{0}. \quad (40)$$

Accordingly, a solution $\delta\Phi$ exists and can be balanced once the term Ψ has been put into the form

$$\Psi = \mathbf{G}_1 \psi_1 + \mathbf{G}_2 \psi_2, \quad (41)$$

where

$$\mathbf{G}_1 = \begin{bmatrix} -\mathbf{z}_1 & -\mathbf{z}_2 & -\mathbf{z}_3 \\ \mathbf{z}_1 & \mathbf{z}_2 & \mathbf{z}_3 \\ 0 & 0 & 0 \\ 0 & 0 & 0 \end{bmatrix}, \quad \mathbf{G}_2 = \begin{bmatrix} -\bar{\mathbf{z}}_1 & -\bar{\mathbf{z}}_2 & -\bar{\mathbf{z}}_3 \\ \bar{\mathbf{z}}_1 & \bar{\mathbf{z}}_2 & \bar{\mathbf{z}}_3 \\ -a - \ell/2 & -a - \ell/2 & -a - \ell/2 \\ -a - \ell/2 & -a - \ell/2 & -a - \ell/2 \end{bmatrix}, \quad (42)$$

given that $\mathbf{C}'_0 = [\mathbf{G}_1 \quad \mathbf{G}_2]$. A straightforward calculation then shows that

$$\psi_1 = k_l \begin{bmatrix} 0 \\ -\langle \mathbf{z}_2, \partial_2 \mathbf{U} \rangle \\ \langle \mathbf{z}_3, \partial_1 \mathbf{U} \rangle \end{bmatrix} + 2k_l \begin{bmatrix} w_1 \\ w_2 \\ w_3 \end{bmatrix} \varphi, \quad (43)$$

and

$$\psi_2 = k_s \begin{bmatrix} 0 \\ -\langle \bar{\mathbf{z}}_2, \partial_2 \mathbf{U} \rangle \\ \langle \bar{\mathbf{z}}_3, \partial_1 \mathbf{U} \rangle \end{bmatrix} + k_s a \begin{bmatrix} 0 \\ \partial_2 \varphi \\ -\partial_1 \varphi \end{bmatrix} + \frac{k_s \ell}{2} \begin{bmatrix} 0 \\ \partial_2 \varphi \\ -\partial_1 \varphi \end{bmatrix}. \quad (44)$$

Therefore, the solution is

$$\delta\Phi = \Gamma_1 \psi_1 + \Gamma_2 \psi_2, \quad (45)$$

where

$$\Gamma_1 = \frac{1}{k_l + k_s} \begin{bmatrix} \frac{2}{3\sqrt{3}} \bar{\mathbf{z}}_2 & \frac{2}{3\sqrt{3}} \bar{\mathbf{z}}_3 & \frac{2}{3\sqrt{3}} \bar{\mathbf{z}}_1 \\ \frac{2}{3\sqrt{3}} \bar{\mathbf{z}}_3 & \frac{2}{3\sqrt{3}} \bar{\mathbf{z}}_1 & \frac{2}{3\sqrt{3}} \bar{\mathbf{z}}_2 \\ 1 & 1 & 1 \\ -1 & -1 & -1 \end{bmatrix}, \quad (46)$$

and

$$\Gamma_2 = \frac{1}{k_l + k_s} \begin{bmatrix} \frac{-2}{3\sqrt{3}} \mathbf{z}_2 & \frac{-2}{3\sqrt{3}} \mathbf{z}_3 & \frac{-2}{3\sqrt{3}} \mathbf{z}_1 \\ \frac{-2}{3\sqrt{3}} \mathbf{z}_3 & \frac{-2}{3\sqrt{3}} \mathbf{z}_1 & \frac{-2}{3\sqrt{3}} \mathbf{z}_2 \\ \frac{k_l+k_s}{6k_s(a+\ell/2)} & -\frac{k_l+k_s}{6k_s(a+\ell/2)} & -\frac{k_l+k_s}{6k_s(a+\ell/2)} \\ -\frac{k_l+k_s}{6k_s(a+\ell/2)} & -\frac{k_l+k_s}{6k_s(a+\ell/2)} & -\frac{k_l+k_s}{6k_s(a+\ell/2)} \end{bmatrix}. \quad (47)$$

It is worth mentioning that the first-order displacement $\delta\Phi$ is not unique and can be modified by addition of an arbitrary periodic zero mode $\mathbf{D}\delta\mathbf{U} + \mathbf{T}\delta\varphi$. However, these two terms will play no further role and can be set to zero with no loss of generality.

3.4. Macroscopic motion equation

Keeping the second-order terms in the equation of motion yields

$$\begin{aligned} -\mathbf{C}'_{l0} \mathbf{K} \mathbf{C}_0 \delta^2\Phi - \mathbf{C}'_{l0} \mathbf{K} (\delta_w \mathbf{C} + \delta_x \mathbf{C} + \delta_\ell \mathbf{C}) \delta\Phi - (\delta_w \mathbf{C} + \delta_x \mathbf{C})' \mathbf{K} \mathbf{C}_0 \delta\Phi \\ - (\delta_w \mathbf{C} + \delta_x \mathbf{C})' \mathbf{K} (\delta_w \mathbf{C} + \delta_x \mathbf{C} + \delta_\ell \mathbf{C}) \Phi_0 - \mathbf{E}_b \mathbf{K}_b \mathbf{C}_b \Phi_0 + \mathbf{F} = -\omega^2 \mathbf{G} \Phi_0. \end{aligned} \quad (48)$$

Therein, we have omitted second-order corrections to the compatibility operator as these will have no influence in the following.

A solution $\delta^2\Phi$ exists if and only if the orthogonality conditions are enforced. The first one reads

$$\begin{aligned} -\mathbf{D}' (\delta_w \mathbf{C} + \delta_x \mathbf{C})' \mathbf{K} \mathbf{C}_0 \delta\Phi - \mathbf{D}' (\delta_w \mathbf{C} + \delta_x \mathbf{C})' \mathbf{K} (\delta_w \mathbf{C} + \delta_x \mathbf{C} + \delta_\ell \mathbf{C}) \Phi_0 \\ - \mathbf{D}' \mathbf{E}_b \mathbf{K}_b \mathbf{C}_b \Phi_0 + \mathbf{D}' \mathbf{F} = -\omega^2 \mathbf{D}' \mathbf{G} \Phi_0. \end{aligned} \quad (49)$$

The second is

$$\begin{aligned} -\mathbf{T}'(\delta_w \mathbf{C} + \delta_x \mathbf{C})' \mathbf{K} \mathbf{C}_0 \delta \Phi - \mathbf{T}'(\delta_w \mathbf{C} + \delta_x \mathbf{C})' \mathbf{K} (\delta_w \mathbf{C} + \delta_x \mathbf{C} + \delta_\ell \mathbf{C}) \Phi_0 \\ - \mathbf{T}' \mathbf{E}_b \mathbf{K}_b \mathbf{C}_b \Phi_0 + \mathbf{T}' \mathbf{F} = -\omega^2 \mathbf{T}' \mathbf{G} \Phi_0. \end{aligned} \quad (50)$$

Both equations involve the leading-order displacements spanned by translations \mathbf{U} and the twisting motion φ and can be interpreted as a pair of macroscopic motion equations. Next, these equations will be rewritten in a form of strain and stress, and reveal the constitutive law that relates them.

3.5. Microtwist continuum and its parity asymmetry

By injecting the related expressions in Section 3.2 into Eqs. (49) and (50), the motion equations of the microtwist continuum can be recast into the form

$$\begin{aligned} -\omega^2 \rho \mathbf{U} &= \mathbf{F} + \nabla \cdot (\mathbf{L} : \nabla^s \mathbf{U} + \mathbf{B} \cdot \nabla \varphi + \mathbf{M} \varphi), \\ -\omega^2 \eta \varphi &= \tau + \nabla \cdot (\mathbf{B}_1 : \nabla^s \mathbf{U} + \mathbf{H} \cdot \nabla \varphi + \mathbf{A} \varphi) \\ &\quad - \mathbf{M}_1 : \nabla^s \mathbf{U} - \mathbf{A}_1 \cdot \nabla \varphi - Q \varphi, \end{aligned} \quad (51)$$

where $\nabla^s \mathbf{U}$ is the symmetric part of the macroscopic displacement gradient, $\nabla \varphi$ is the twisting gradient, the dots \cdot and $:$ symbolize simple and double contraction of tensors and $\nabla \cdot$ is the divergence operator, and the effective tensors \mathbf{L} , \mathbf{B} , \mathbf{B}_1 , \mathbf{A} , \mathbf{A}_1 , \mathbf{M} , \mathbf{M}_1 and \mathbf{H} are obtained in functions of the geometry parameters of the lattice and effective stiffnesses of the hinge given in Appendix C. ρ and η are mass density and moment of inertia density

$$\rho = \frac{1}{A} \sum_i m_i, \quad \eta = \frac{1}{A} \sum_i I_i, \quad (52)$$

where $A = 6\sqrt{3}a^2$ is the area of a unit cell. The vector–scalar pair (\mathbf{F}, τ) is the resultant force–torque acting on a unit cell per unit cell area, which read

$$\mathbf{F} = \frac{1}{A} \sum_i \mathbf{F}_i, \quad \tau = \frac{1}{A} (M_2 - M_1). \quad (53)$$

The macroscopic motion equation then can be written as the balance equations

$$-\omega^2 \rho \mathbf{U} = \mathbf{F} + \nabla \cdot \boldsymbol{\sigma}, \quad -\omega^2 \eta \varphi = \tau + \nabla \cdot \boldsymbol{\xi} + s, \quad (54)$$

where $\boldsymbol{\sigma}$, $\boldsymbol{\xi}$ and s are second, first and zero-order tensorial stress measures related to the strain measures $\nabla^s \mathbf{U}$, $\nabla \varphi$ and φ through the macroscopic constitutive law

$$\begin{bmatrix} \boldsymbol{\sigma} \\ \boldsymbol{\xi} \\ -s \end{bmatrix} = \begin{bmatrix} \mathbf{L} & \mathbf{B} & \mathbf{M} \\ \mathbf{B}_1 & \mathbf{H} & \mathbf{A} \\ \mathbf{M}_1 & \mathbf{A}_1 & Q \end{bmatrix} \begin{bmatrix} \nabla^s \mathbf{U} \\ \nabla \varphi \\ \varphi \end{bmatrix}. \quad (55)$$

Thus, a 2D microtwist continuum with extra DOFs and additional measures of strain, stress, and inertia have already been derived, which can describe the global behavior of a hinged Kagome lattice in the homogenization limit. It can be concluded that the effective tensors \mathbf{M} , \mathbf{M}_1 , \mathbf{A} and \mathbf{A}_1 are responsible for P-asymmetry because they are odd functions of the w_j . Following the approach as one in the spring–mass model (Nassar et al., 2020a; Xia et al., 2021), the polarization direction which depends on the distortion parameters w_j is given by

$$\mathbf{P} = \frac{1}{2} \sum_j \text{sgn}(w_j) \mathbf{r}_j. \quad (56)$$

It is worth noting here, the polarized mechanical behavior is immune to spatial differences in the radius of curvature at the hinge and the distortion of lattices, small and large, as long as the signs of distortion parameters remain unchanged.

3.6. Dispersion relations

Having derived the equations of a microtwist continuum modeling weakly-distorted Kagome lattices with elastic hinges, it is now to inquire whether the continuum is faithful in its prediction of low-frequency wave propagation and dispersion. We will focus on investigation of the first three fundamental wave branches based on the assumption of the microtwist theory.

First, we conduct a numerical characterization of hinged lattices in Figs. 3a and 3b using finite element analysis and Bloch periodic boundary conditions (Details of the geometrical and material properties in the calculation can be found in Appendix D). Dispersion relations of the hinged regular lattice and polarized lattice II are presented in Figs. 3c and 3d, respectively. Recall that dispersion relations of regular Kagome lattices with idealized hinges feature zero-frequency modes (Nassar et al., 2020a). Here, in contrast, as the elastic hinges prevent the rigid triangles from rotating freely with respect to one another, we do not find any zero-frequency modes except at zero wave number Γ . We then consider that plane waves are propagating through the discrete Kagome lattices. There exists at specific frequencies ω and wavenumbers \mathbf{q} solution to the dispersion relation

$$\det \{ [\mathbf{C}_l(\mathbf{q})' \mathbf{K} (\mathbf{C}_l(\mathbf{q}) + \mathbf{C}_e(\mathbf{q}))] + \mathbf{E}_b(\mathbf{q}) \mathbf{K}_b \mathbf{C}_b(\mathbf{q}) - \omega^2 \mathbf{G} \} = 0. \quad (57)$$

The discrete Kagome lattice has six DOFs per unit cell so that there are six solution frequencies for any given wavenumber \mathbf{q} . At last, we consider that an infinite microtwist continuum under a plane wave in x-direction, the dispersion relations are obtained by injecting translational displacements \mathbf{U} and the twisting angle φ

$$\mathbf{U}(\mathbf{x}, t) = \mathbf{U}_0 \exp(i \langle \mathbf{q}, \mathbf{x} \rangle - i\omega t), \quad \varphi(\mathbf{x}, t) = \varphi_0 \exp(i \langle \mathbf{q}, \mathbf{x} \rangle - i\omega t), \quad (58)$$

into Eq. (51) under zero resultant force-torque. Figs. 3c and 3d respectively show the dispersion curves of regular lattice and polarized lattice II (see Appendix A), predicted by employing the discrete (green dotted lines) and microtwist (red dashed lines) models. Both plots show the microtwist continuum produces three branches corresponding to the coupled translational and rotational waves, and agrees well with those given by the exact hinged and discrete models up to frequencies comparable to the cutoff frequencies and those for small to medium wavenumbers.

3.7. Zero modes

For the finite hinged Kagome lattice, we perform modal analyses at lowest frequency (approximate zero) to investigate location or distribution of zero modes in terms of the total displacement in two types of hinged Kagome lattices: regular lattice and polarized lattice II (see Appendix A). We then quantitatively compare the prediction from the hinged lattice model with 47×11 unit cells in Figs. 4a and 4b and the microtwist continuum model in Figs. 4c and 4d.

In the simulation, all the DOFs are fixed on the top and bottom boundaries for the finite models shown in Fig. 4. From the comparison, we can conclude that the developed microtwist continuum theorem is capable of quantitatively capturing distribution of bulk and edge zero modes for different hinged Kagome lattices: the regular Kagome lattice only has bulk zero modes (Figs. 4a and 4c); the polarized Kagome lattice II has asymmetric zero modes which is localized near the left boundary and decays exponentially towards the bulk (Figs. 4b and 4d). The emergence of polarization phenomenon is a symptom of the loss of parity symmetry, which will be further validated and discussed in the following section.

4. Experimental validation

The present section deals with an experimental validation of the microtwist continuum model in Section 3, against the results of static

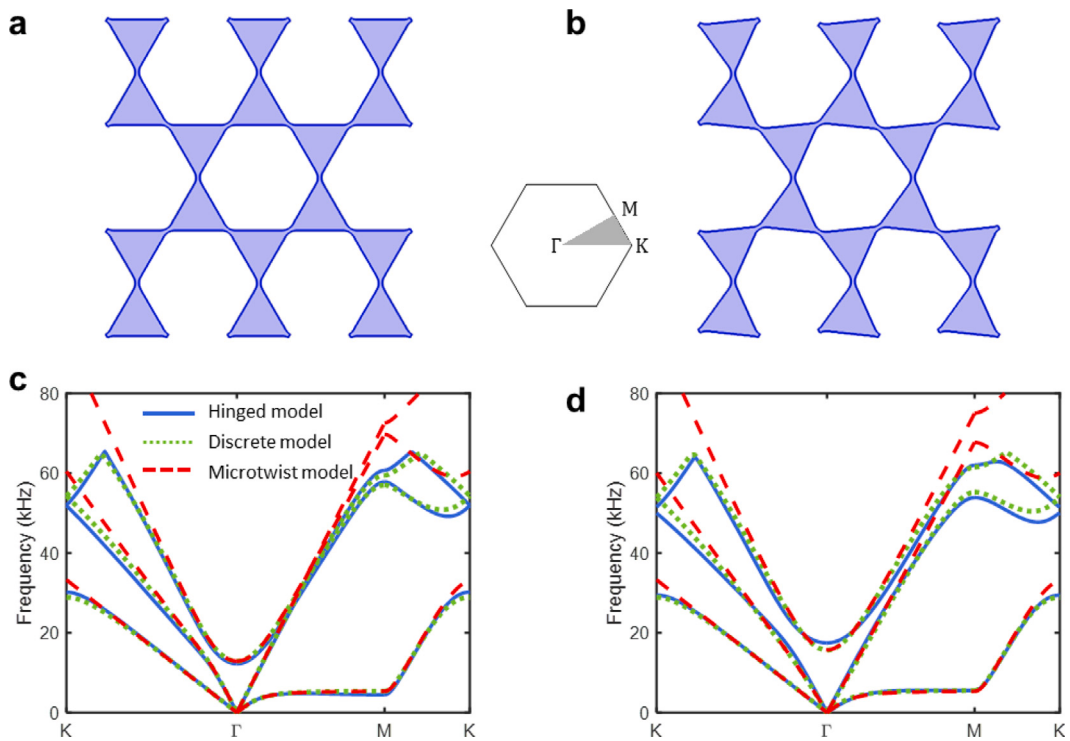


Fig. 3. Examples of regular (a) and polarized (b) Kagome lattices, and of their respective dispersion diagrams (c) and (d). Blue solid, green dotted and red dashed lines correspond to the dispersion relations of the hinged, discrete and microtwist modes, respectively. The inset show the first Brillouin zone with symmetry points Γ , M and K of (a) and (b). Note that the lattice parameters are $(0, 0, 0, 0)$ in (a) and $(-0.03, -0.03, 0.03, 0)$ in (b).

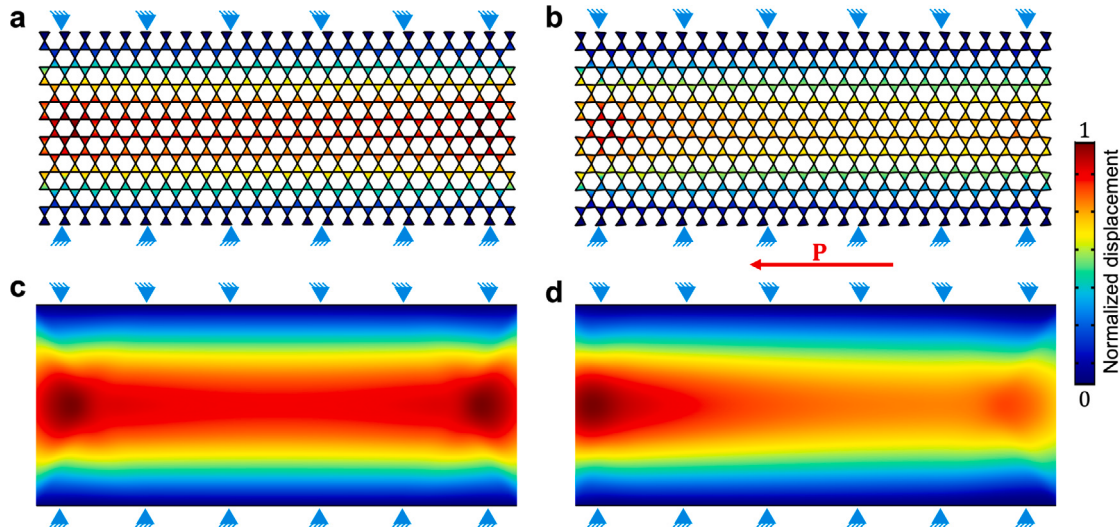


Fig. 4. Modal analyses of regular (a, c) and polarized (b, d) Kagome lattices and of their respective zero modes by employing the hinged lattice model (a, b) and the microtwist continuum model (c, d). The top and bottom boundaries are fixed, while the left and right boundaries are free. The displacement magnitudes are normalized by the largest value calculated in the mode field. Note that the lattice parameters are $(0, 0, 0, 0)$ in (a) and (c), and $(-0.03, -0.03, 0.03, 0)$ in (b) and (d). The red arrow show the polarization direction of (b) and (d).

indentation and three-point bending tests on physical samples (Details of the sample manufacturing, numerical simulation, and experiment test can be found in Appendix D and Appendix E).

4.1. Parity asymmetric indentation responses

We first examine the indentation response of a regular plate along the vertical direction shown in Fig. 5a by using a MTS Landmark 370 servo-hydraulic system. Samples comprising 28×31 triangles are fixed on the left and right boundaries. Using a compression test

machine MTS, we indent the plate at the center of top/bottom boundary by moving for a fixed distance and measure the reaction force. Fig. 5b compares the experimental, numerical and microtwist force-displacement responses of such sample, highlighting an overall satisfactory agreement among the three methods. In order to further qualitatively investigate the mechanical behavior in the regular lattice, the static vertical displacement fields are extracted from the numerical simulation of hinged model (Fig. 5c), the DIC measurement (Fig. 5d) and the microtwist model (Fig. 5e). The three plots match satisfactorily and validate the microtwist elasticity theory.

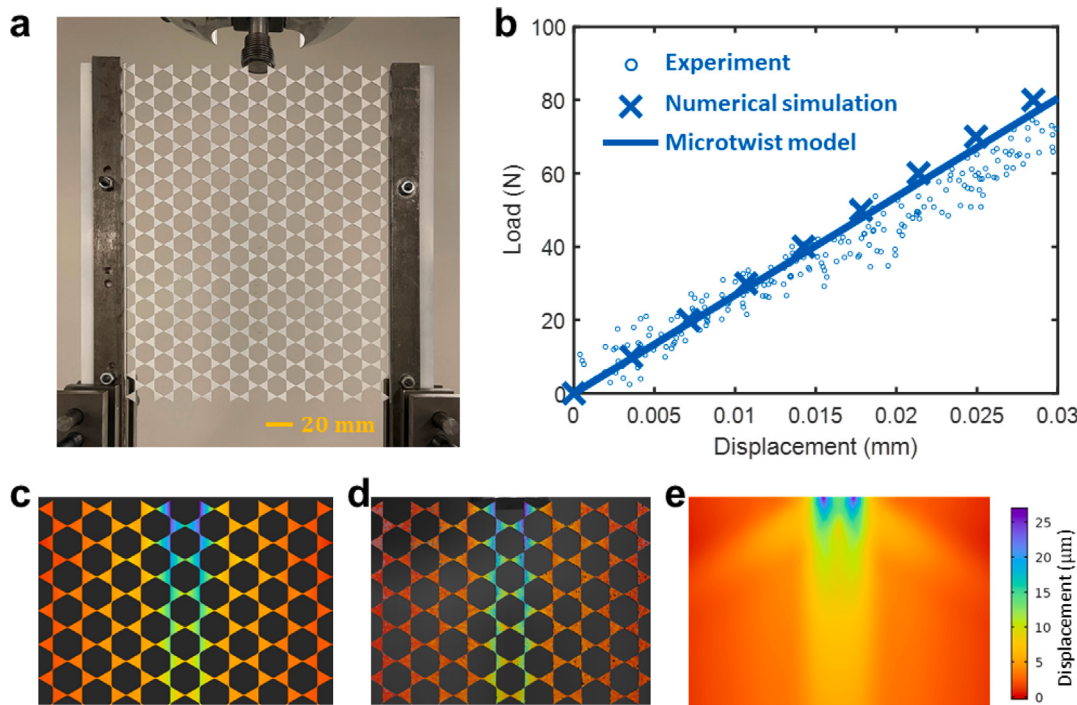


Fig. 5. Calculated and measured results of regular Kagome lattice under indentation test. (a) Photograph of the regular plate sample under indentation test. (b) Measured and calculated vertical displacements of triangles on the top row. Scale bar, 20 mm. The blue circles, blue crosses, solid blue lines result from the experimental measurement, numerical simulation, and microtwist model, respectively. (c) Vertical displacement field from the numerical simulation of the hinged model. (d) Vertical displacement field from the DIC measurement. (e) Vertical displacement field from the microtwist model.

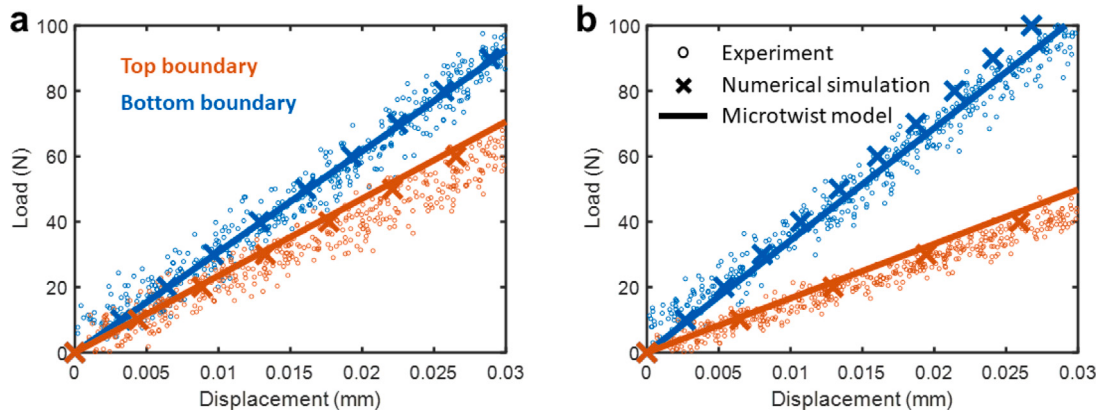


Fig. 6. Calculated and measured results of Polarized Kagome lattice I (a) and II (b) under indentation test. Orange (blue) symbols denote the data obtained from the indentation test on the top (bottom) boundary. The circles, crosses, solid lines result from the experimental measurement, numerical simulation, and microtwist model, respectively.

We then perform static indentation tests on two opposing boundaries of finite polarized lattices I and II to demonstrate difference in their mechanical responses and the emergence of P-asymmetric effects. Figs. 6a and 6b show the asymmetric indentation responses, which have the excellent agreement among the numerical simulations, the experimental tests and the microtwist theory. Also by comparing these two plots, it should be interesting to mention that the stiffness bias of the hard and soft boundaries is significantly increased with the increase of the distortion parameters. It illustrates the potential benefit of incorporating distortion parameters into designs of configurable P-asymmetric materials.

4.2. Parity asymmetric bending behaviors

Thus far, we have demonstrated P-asymmetry in the polarized microtwist medium under indentation. However, it should be noted that

this property is not limited to this loading condition. To this end, we now examine the elastic response of the polarized beam II under three-point bending test, as shown in Fig. 7 (Elastic responses of the regular beam and the polarized beam I can be found in Appendix F). Using test machine MTS, the polarized beam is mounted in a three-point bending configuration and a 50 N loading is applied at the top center of the lattice. We then use DIC system to measure the vertical displacements of triangles on the top row. The resulting data is shown in Fig. 7b, where the vertical displacements are plotted against the horizontal coordinate x . Our experimental measurement, numerical simulation and microtwist model demonstrate that there exists an asymmetric bending curve in the polarized lattice-based beam. We further plot the vertical displacement field by extracting from the numerical simulation (Fig. 7c), the DIC measurement (Fig. 7d) and the microtwist model (Fig. 7e). These three plots have good agreement and demonstrate polarized responses in the microtwist medium as well.

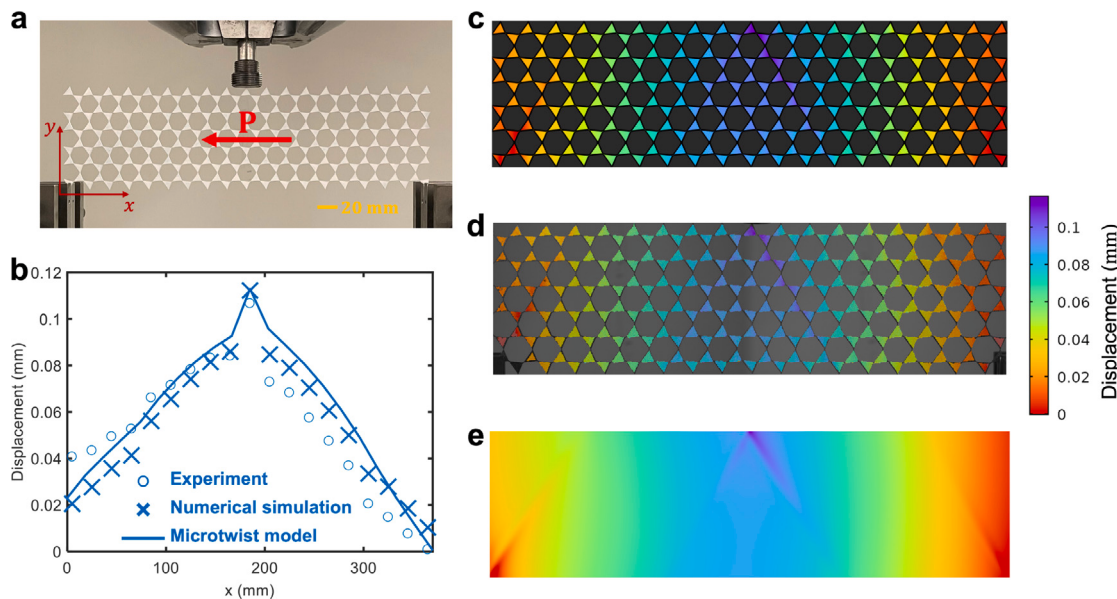


Fig. 7. Calculated and measured results of the Polarized beam II under three-point bending test with 50 N loading. (a) Photograph of the beam sample under three-point bending test. Scale bar, 20 mm. (b) Measured and calculated vertical displacements of triangles on the top row. The blue circles, blue crosses, solid blue lines result from the experimental measurement, numerical simulation, and microtwist model, respectively. (c) Vertical displacement field from the numerical simulation of the hinged model. (d) Vertical displacement field from the DIC measurement. (e) Vertical displacement field from the microtwist model.

5. Exotic behavior under static and dynamic loadings

Microtwist media with zero modes can also possess exotic behavior due to the microtwisting under static and dynamic loadings that cannot be observed in conventional elasticity. In this section, we will investigate nonuniform static deformations and parity asymmetric surface wave propagation in weakly-distorted hinged Kagome lattices. Results are derived from the numerical simulation of hinged models and the microtwist model.

5.1. Nonuniform deformations under complex static loadings

We consider a distorted Kagome plate with lattice parameters $(x_1, x_2, x_3, z) = (0.05, 0.05, 0.05, 0)$, as shown in Fig. 8a. Four constant displacements (red arrows, $|u_x| = |u_y| = 20 \text{ mm}$) are prescribed at four corners as global “pure shear” via compression along one direction and expansion along the other. Figs. 8b and 8c respectively present the horizontal and vertical displacement profiles calculated by the hinged lattice model (left), the microtwist continuum (middle) and the Cauchy continuum (right; Details of Cauchy continuum can be found in Appendix G). The displacement components U_x and U_y from the Cauchy continuum are symmetrically distributed. However, the displacement patterns predicted from the hinged model and the microtwist continuum are no longer symmetrically distributed. Therefore, the microtwist continuum theory is able to accurately capture the displacement components by considering the contribution from the microtwisting while the conventional Cauchy theory fails.

5.2. Parity asymmetric surface wave distribution

As one application of zero modes in elastic hinged Kagome lattices, we also study polarized surface propagation on the free boundary of the microtwist medium. These parity asymmetric surface modes in the finite microtwist medium present a new class of surface waves have not been explored in the theories of conventional elasticity. To this end, we conduct a complete numerical characterization of a polarized Kagome lattice with parameters $(x_1, x_2, x_3, z) = (-0.03, -0.03, 0.03, 0)$. In the simulation, the supercell is composed of a 2×17 array of unit cells and is terminated by a free boundary at the top and bottom

and Floquet–Bloch boundary conditions along the x direction. Fig. 9a shows the dispersion diagram resulting from the numerical simulation of hinged model (blue solid lines) and microtwist model (red circles). We recognize the emergence of two new branches lower than the dispersive region of the lowest bulk band (gray area). It agrees well with the two lowest dispersion curves given by the exact hinged model and the microtwist model and a discrepancy between these two models is found in a relative higher frequency regime. This is understandable because the assumptions of the perturbation approach are used; see Section 3.1. The mode shapes shown in Figs. 9b and 9c, calculated along the lowest two branches, feature parity asymmetric distribution at one soft boundary as expected by the polarization direction, because a significant amount of displacement is observed at the soft side. This result qualifies these branches as edge modes and characterizes the upper edge as the soft boundary, consistent with the polarization vector predictions. It is worth stressing that the edge modes evolving from zero-frequency modes of the topological polarized Kagome lattice are different from those in the dynamic regime (Ma et al., 2019). The fact that the microtwist media feature parity-asymmetric surface wave distribution constitutes an interesting departure from the conventional case of Rayleigh waves in the Cauchy medium. Finally, it is of interest to explore the tunable parity asymmetric surface waves in microtwist media under the external stimulus, such as mechanical (Chen et al., 2021) and electrical (Li et al., 2021; Zhou et al., 2020) loads.

6. Conclusion

In this paper, we develop a microtwist elasticity theory of hinged Kagome lattices to capture the polarized mechanical behavior by modeling the hinge as a flexible beam. Performance of the proposed theory is validated against the exact hinged lattice model in a number of problems including predicting the dispersion relations and the parity asymmetric distribution of zero modes. Furthermore, experimental and numerical validations on the polarized indentation and bending responses are provided for the first time. At last, we demonstrate exotic behavior of the microtwist medium under nonuniform boundary deformations and parity asymmetric surface wave propagation. We believe the theory opens new pathways for the designs of hinged metamaterials in the linear regime to capture the polarized behavior. We also hope to

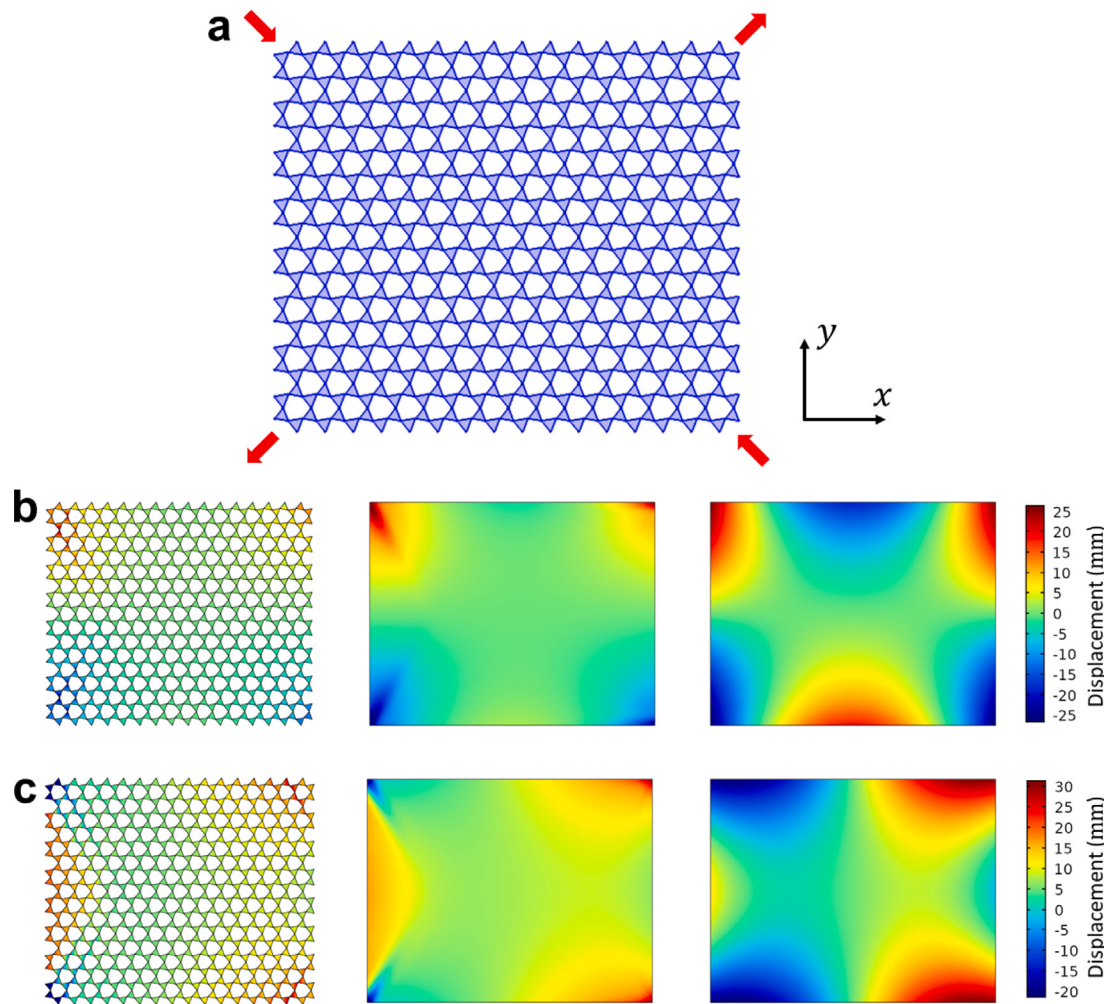


Fig. 8. Nonuniform deformations under complex loading conditions. (a) Applying fixed deformations ($|U_x| = |U_y| = 20$ mm) at four corners of the pre-twisted Kagome lattice. (b) Horizontal displacement fields, U_x . (c) Vertical displacement fields, U_y . Left, middle and right correspond to the hinged, microtwist and Cauchy models.

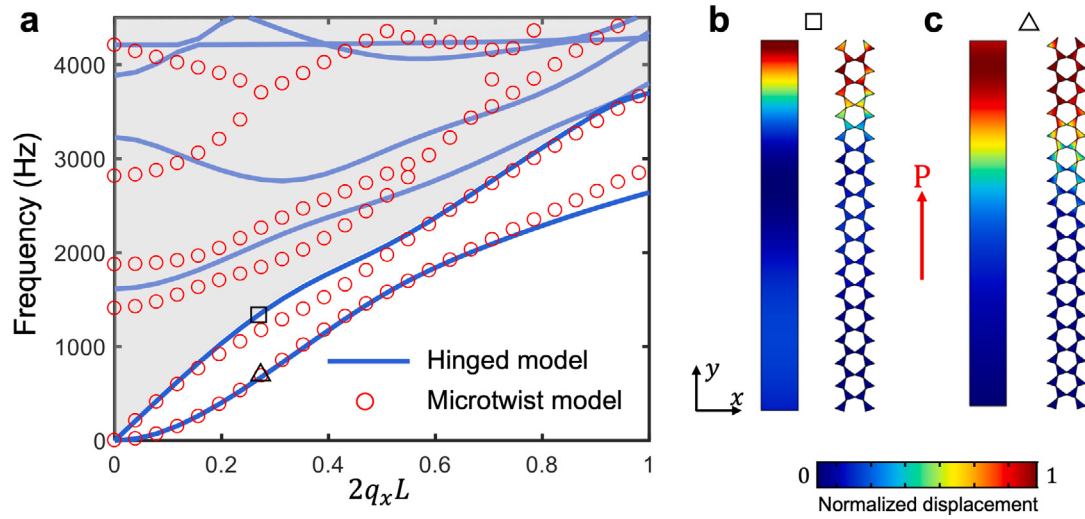


Fig. 9. (a) Dispersion diagram for a supercell under free boundary conditions at the top and bottom and periodic boundary conditions in the x direction. The lattice parameters are $(-0.03, -0.03, 0.03, 0)$ and the polarization direction is towards the top boundary. The solid blue lines and red circles result from the hinged and microtwist model, respectively. The gray areas are bulk bands, while the lowest two branches are surface wave bands. (b, c) Surface mode shapes of the supercell for the lowest two branches result from the microtwist (left) and hinged (right) models. The displacement magnitudes are normalized by the largest value calculated in the wave field.

see in the near future that the microtwist theory could be generalized by taking the geometrical and material nonlinearities into account, and

will be applied to strongly distorted lattices with soft or soft and hard mixed materials.

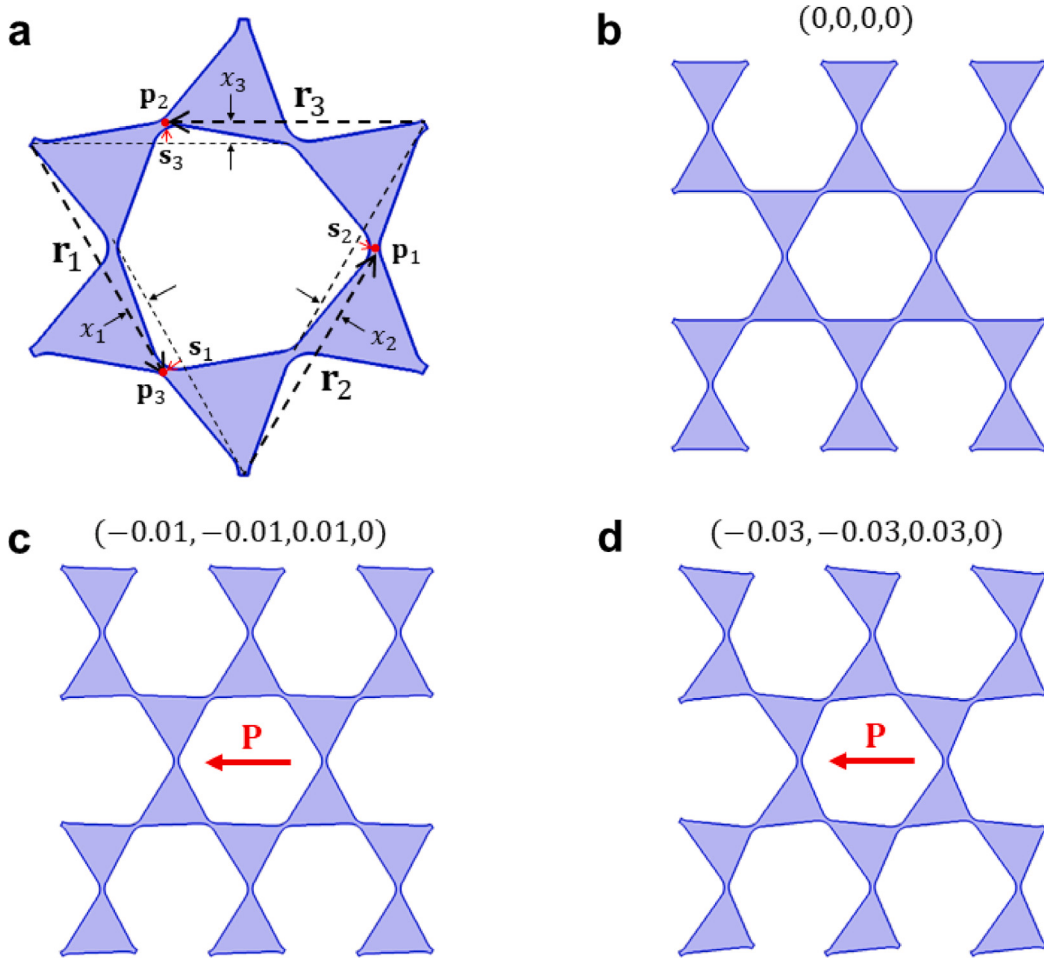


Fig. A.1. Kagome lattice model. (a) An annotated lattice; (b) Regular lattice $(0,0,0,0)$; (c) Polarized lattice I $(-0.01, -0.01, 0.01, 0)$; (d) Polarized lattice II $(-0.03, -0.03, 0.03, 0)$. Red arrows show the polarization direction, $\mathbf{P} = \mathbf{r}_3$.

Acknowledgments

This work is supported by the NSF CMMI, USA under Award No. 1930873 with Program Manager Dr. Nakhiah Goulbourne, the Air Force Office of Scientific Research, USA under Grant No. AF 9550-18-1-0342 and AF 9550-20-0279 with Program Manager Dr. Byung-Lip (Les) Lee and the Army Research Office, USA under Grant No. W911NF-18-1-0031 with Program Manager Dr. Daniel P. Cole.

Appendix A. Characterization of Kagome lattices

For the lattice characterization, we use the description in (Kane and Lubensky, 2014). The Kagome lattice in Fig. A.1 are defined by its Bravais lattices with primitive lattice vectors

$$\mathbf{r}_j = 2L \left(\cos \frac{2j-3}{3}\pi, \sin \frac{2j-3}{3}\pi \right), \quad j \in \{1, 2, 3\}, \quad (\text{A.1})$$

where L is the half of lattice constant. The unit cells are described by four parameters (x_1, x_2, x_3, z) , where x_j and z denote the buckling of the line of bonds along \mathbf{r}_j and the asymmetry in the sizes of the two triangles, respectively. The lattice sites are then obtained as follows:

$$\begin{aligned} \mathbf{p}_1 &= \mathbf{r}_1/2 + \mathbf{s}_2, \\ \mathbf{p}_2 &= \mathbf{r}_2/2 - \mathbf{s}_1, \\ \mathbf{p}_3 &= \mathbf{r}_3/2, \end{aligned}$$

where \mathbf{s}_j denotes the displacement of \mathbf{p}_{j-1} relative to the midpoint of the line along \mathbf{r}_j and can be described by

$$\begin{aligned} \mathbf{s}_1 &= x_1(\mathbf{r}_3 - \mathbf{r}_2) + y_1\mathbf{r}_1, \\ \mathbf{s}_2 &= x_2(\mathbf{r}_1 - \mathbf{r}_3) + y_2\mathbf{r}_2, \\ \mathbf{s}_3 &= x_3(\mathbf{r}_2 - \mathbf{r}_1) + y_3\mathbf{r}_3, \end{aligned} \quad (\text{A.2})$$

with

$$\begin{aligned} y_1 &= z/3 + x_3 - x_2, \\ y_2 &= z/3 + x_1 - x_3, \\ y_3 &= z/3 + x_2 - x_1. \end{aligned} \quad (\text{A.3})$$

In this paper, three Kagome lattices are chosen: regular lattice $(0,0,0,0)$ in Fig. A.1b, polarized lattice I $(-0.01, -0.01, 0.01, 0)$ in Fig. A.1c, and polarized lattice II $(-0.03, -0.03, 0.03, 0)$ in Fig. A.1d. Note that the red arrows in Figs. A.1c and A.1 d are polarization vectors (Kane and Lubensky, 2014). Note also, that for the weakly-distorted Kagome lattices $w_j = \text{sgn}(x_j) \|\mathbf{s}_j\| / \sqrt{3}$.

Appendix B. Characterization of hinge deformation

In the limit that $w_0 \ll L$, the hinge will become very flexible compared to the stiff triangle pieces. Therefore, the large triangle elements are approximated as rigid bodies and all strain deformation is assumed to take place at the hinges. We then refer to the elastic hinge between two triangles as a beam with varying cross-section areas, as shown in Fig. A.2 (Day et al., 1992; Coulais, 2016; Liang and Crosby, 2020). Here, the stretching of beam is governed by a stretching stiffness

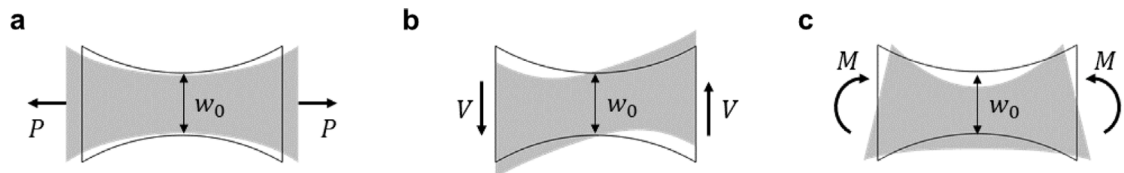


Fig. A.2. Three deformation modes of the hinge. (a) Stretching; (b) Pure Shear; (c) Pure Bending.

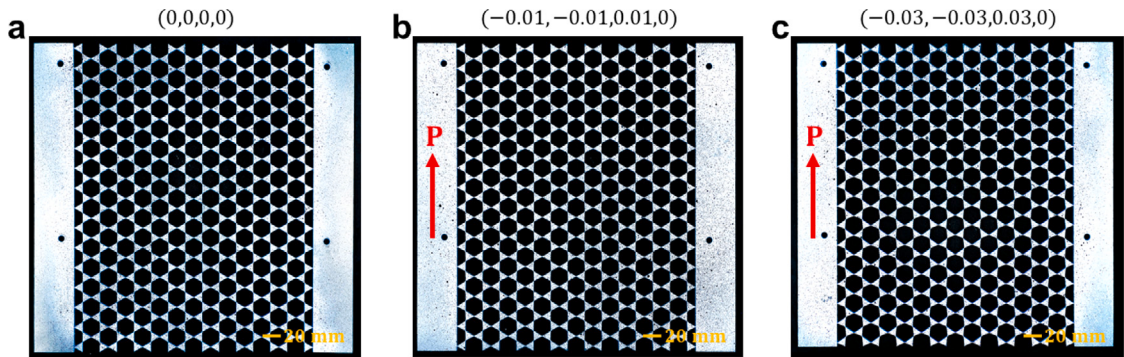


Fig. A.3. Photograph of three samples for indentation tests. (a) Regular plate with lattice parameters $(0,0,0,0)$; (b) Polarized plate I with lattice parameters $(-0.01,-0.01,0.01,0)$; (c) Polarized plate II with lattice parameters $(-0.03,-0.03,0.03,0)$. Red arrows show the polarization vectors towards the top boundary. Scale bars, 20 mm.

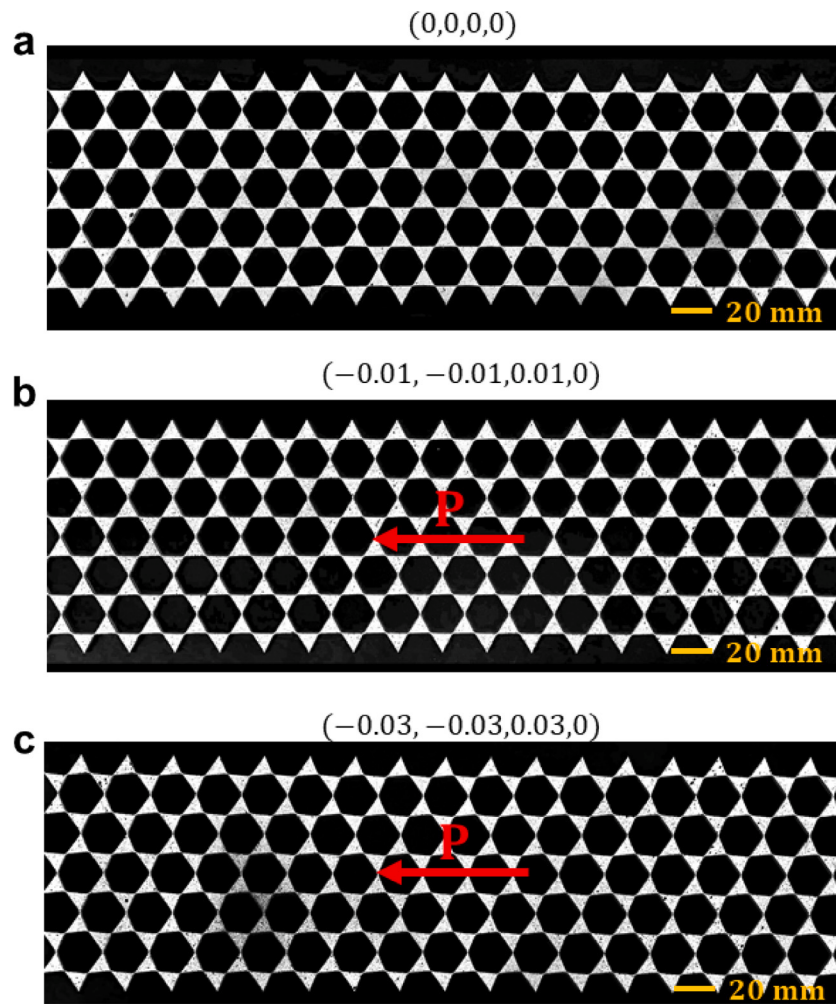


Fig. A.4. Photograph of three samples for three-point bending tests. (a) Regular beam with lattice parameters $(0,0,0,0)$; (b) Polarized beam I with lattice parameters $(-0.01,-0.01,0.01,0)$; (c) Polarized beam II with lattice parameters $(-0.03,-0.03,0.03,0)$. Red arrows show the polarization vectors towards the left boundary. Scale bars, 20 mm.

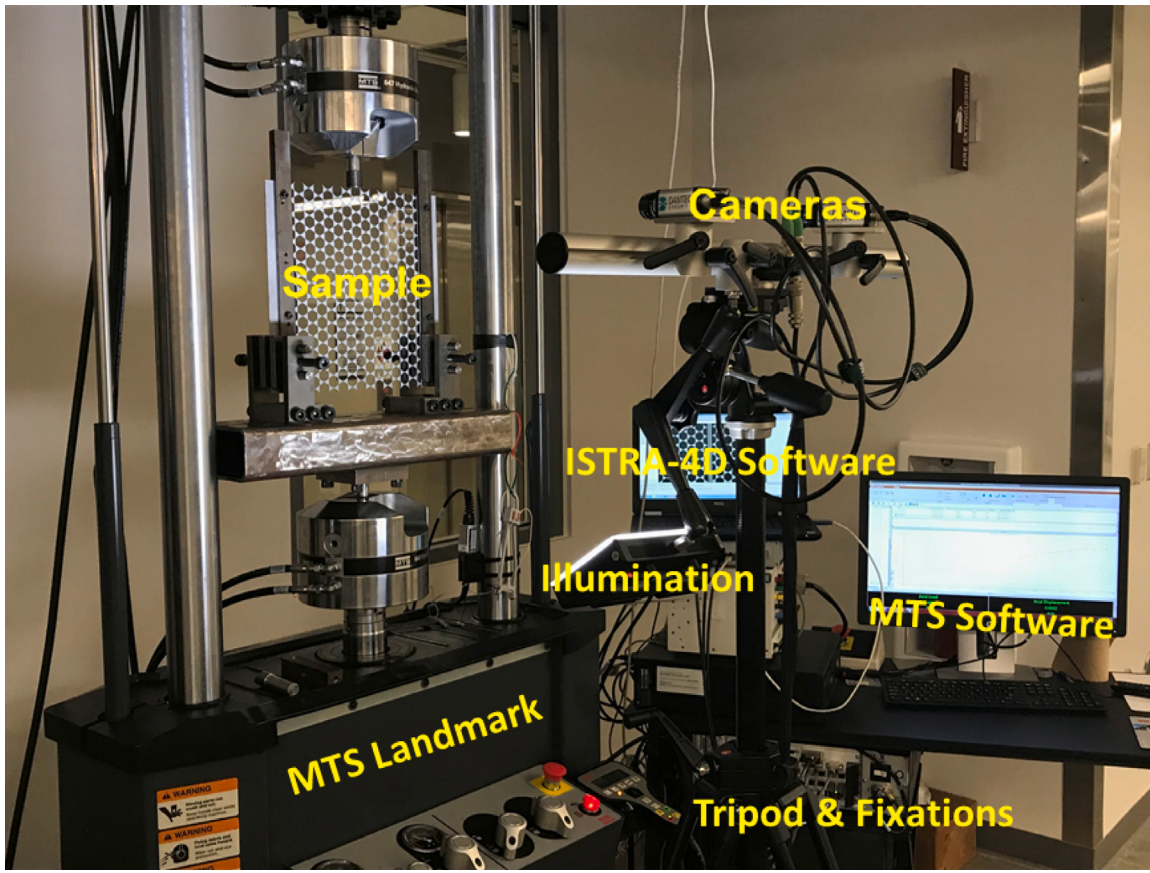


Fig. A.5. Experimental setup for the static test. The indentation and three-point bending loadings are supplied by the MTS system, and the displacement fields are measured by the DIC system.

k_l ; the pure shear of beam is governed by a shear stiffness k_s ; and the pure bending of beam is governed by a bending stiffness k_b . Note that these elastic stiffnesses are independent and can be obtained by applying three sorts of boundary conditions depicted in Fig. A.2, which can be expressed as (Liang and Crosby, 2020)

$$k_l = \frac{Eh}{\pi} \sqrt{\frac{w_0}{r}}, \quad k_s = \frac{Eh}{3\pi} \left(\frac{w_0}{r} \right)^{\frac{3}{2}}, \quad k_b = \frac{2Eh}{9\pi} r^2 \left(\frac{w_0}{r} \right)^{\frac{5}{2}}, \quad (\text{B.1})$$

where h is the thickness of lattice, $w_0 = 2r \left(\frac{1}{\cos \frac{\theta}{6}} - 1 \right) = 0.62$ mm, $k_l = 5.55 \times 10^7$ N/m, $k_s = 5.72 \times 10^6$ N/m, $k_b = 4.72$ N·m. As such, bending stiffness k_b is much smaller than $k_l a^2$ and $k_s a^2$ so that it can be understood as a second-order quantity.

To quantify the energy of hinge deformation, we recall compatibility Eqs. (5), (6) and (7), where the stretching and shear deformation gives $\Delta_{l_j} \sim A_{s_i} \sim a\varphi_j$, and the bending deformation yields $\Delta_{\theta_j} \sim \varphi_j$. Here, we ignore the unit cell index (m, n). Consequently, the stored elastic energy due to bending deformation in the ligament is much smaller than those due to stretching and shear deformation, that is

$$k_b \Delta_{\theta_j}^2 \ll \min\{k_l \Delta_{l_j}^2, k_s \Delta_{s_j}^2\}. \quad (\text{B.2})$$

Appendix C. Effective tensors

The involved effective tensors in Eq. (51) are given by

$$\begin{aligned} \mathbf{L} = \frac{a^2}{A} \left\{ 12k_l(\mathbf{z}_{232\bar{3}} + \mathbf{z}_{32\bar{3}\bar{3}}) + 12k_s(\mathbf{z}_{233\bar{2}} + \mathbf{z}_{32\bar{2}\bar{3}}) \right. \\ \left. + \frac{k_l^2}{k_l + k_s} (-8\mathbf{z}_{\bar{3}22\bar{3}} - 4\mathbf{z}_{\bar{3}23\bar{2}} - 4\mathbf{z}_{\bar{2}32\bar{3}} - 8\mathbf{z}_{\bar{2}33\bar{2}}) \right\}, \end{aligned} \quad (\text{C.4})$$

$$\begin{aligned} &+ \frac{k_l k_s}{k_l + k_s} (4\sqrt{3}\mathbf{z}_{\bar{3}\bar{2}3\bar{2}} - 4\sqrt{3}\mathbf{z}_{\bar{2}\bar{3}2\bar{3}} - 4\sqrt{3}\mathbf{z}_{\bar{3}\bar{2}2\bar{3}} + 4\sqrt{3}\mathbf{z}_{\bar{2}32\bar{3}}) \\ &+ \frac{k_s}{k_l + k_s} [-4(k_l + 3k_s)\mathbf{z}_{\bar{3}\bar{2}\bar{2}\bar{3}} + 4k_l\mathbf{z}_{\bar{3}\bar{2}3\bar{2}} + 4k_l\mathbf{z}_{\bar{2}\bar{3}3\bar{2}} \\ &- 4(k_l + 3k_s)\mathbf{z}_{\bar{2}\bar{3}\bar{3}\bar{2}}] \}, \end{aligned} \quad (\text{C.1})$$

$$\begin{aligned} \mathbf{B} = \frac{a^2}{A} \left\{ -12ak_s(\mathbf{z}_{\bar{3}\bar{2}\bar{3}} + \mathbf{z}_{\bar{2}\bar{3}\bar{2}}) - 6\ell k_s(\mathbf{z}_{\bar{3}\bar{2}\bar{3}} + \mathbf{z}_{\bar{2}\bar{3}\bar{2}}) + \frac{4\sqrt{3}k_l k_s a}{k_l + k_s} (\mathbf{z}_{\bar{3}22} - \mathbf{z}_{23\bar{3}}) \right. \\ &+ \frac{2\sqrt{3}k_l k_s \ell}{k_l + k_s} (\mathbf{z}_{\bar{3}22} - \mathbf{z}_{23\bar{3}}) + \frac{k_s a}{k_l + k_s} [4(k_l + 3k_s)\mathbf{z}_{\bar{3}\bar{2}\bar{3}} - 4k_l\mathbf{z}_{\bar{3}22} \\ &- 4k_l\mathbf{z}_{23\bar{3}} + 4(k_l + 3k_s)\mathbf{z}_{\bar{2}\bar{3}\bar{2}}] + \frac{k_s \ell}{k_l + k_s} [2(k_l + 3k_s)\mathbf{z}_{\bar{3}\bar{2}\bar{3}} - 2k_l\mathbf{z}_{\bar{3}22} \\ &- 2k_l\mathbf{z}_{23\bar{3}} + 2(k_l + 3k_s)\mathbf{z}_{\bar{2}\bar{3}\bar{2}}] \}, \end{aligned} \quad (\text{C.2})$$

$$\begin{aligned} \mathbf{B}_1 = \frac{a^3}{A} \left\{ -12k_s(\mathbf{z}_{\bar{3}\bar{2}\bar{3}} + \mathbf{z}_{\bar{2}\bar{3}\bar{2}}) + \frac{4\sqrt{3}k_l k_s}{k_l + k_s} (\mathbf{z}_{\bar{3}3\bar{2}} - \mathbf{z}_{22\bar{3}}) \right. \\ &+ \frac{k_s}{k_l + k_s} [4(k_l + 3k_s)\mathbf{z}_{\bar{3}3\bar{2}} - 4k_l\mathbf{z}_{3\bar{2}\bar{2}} - 4k_l\mathbf{z}_{22\bar{3}} \\ &+ 4(k_l + 3k_s)\mathbf{z}_{\bar{2}\bar{3}\bar{2}}] \}, \end{aligned} \quad (\text{C.3})$$

$$\begin{aligned} \mathbf{H} = \frac{a^3}{A} \left\{ 12ak_s(\mathbf{z}_{\bar{2}\bar{2}} + \mathbf{z}_{\bar{3}\bar{3}}) + 6\ell k_s(\mathbf{z}_{\bar{2}\bar{2}} + \mathbf{z}_{\bar{3}\bar{3}}) \right. \\ &- \frac{4k_s a}{k_l + k_s} [(k_l + 3k_s)\mathbf{z}_{\bar{3}\bar{3}} - k_l\mathbf{z}_{\bar{3}\bar{2}} - k_l\mathbf{z}_{\bar{2}\bar{3}} + (k_l + 3k_s)\mathbf{z}_{\bar{2}\bar{2}}] \\ &- \frac{2k_s \ell}{k_l + k_s} [(k_l + 3k_s)\mathbf{z}_{\bar{3}\bar{3}} - k_l\mathbf{z}_{\bar{3}\bar{2}} - k_l\mathbf{z}_{\bar{2}\bar{3}} + (k_l + 3k_s)\mathbf{z}_{\bar{2}\bar{2}}] \}, \end{aligned} \quad (\text{C.4})$$

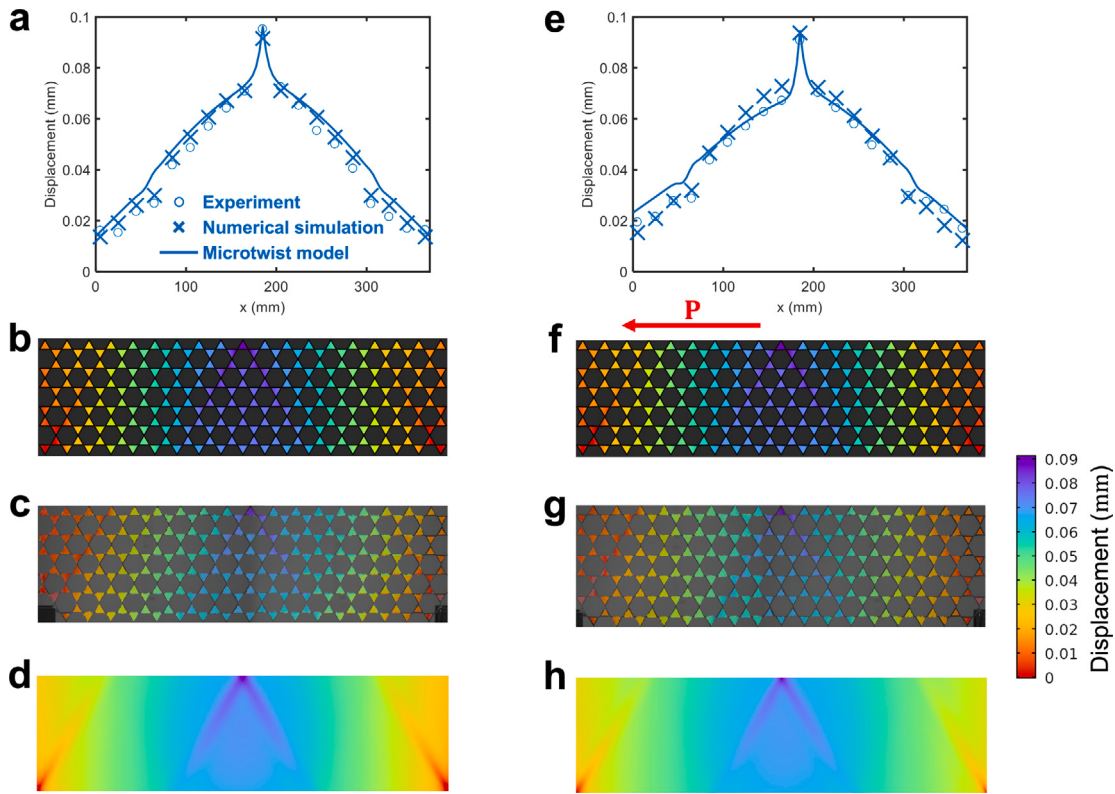


Fig. A.6. Static responses of regular (a-d) and polarized I (e-h) beams under three-point bending tests with 50 N loading. (a, e) Measured and calculated vertical displacements of triangles on the top row. (b, f) Vertical displacement field from the numerical simulation of the hinged model. (c, g) Vertical displacement field from the DIC measurement. (d, h) Vertical displacement field from the microtwist model. The blue circles, blue crosses, solid blue lines result from the experimental measurement, numerical simulation, and microtwist model, respectively.

$$\mathbf{M} = \frac{a}{A} \left\{ 4\sqrt{3}k_l(w_2\mathbf{z}_{\bar{3}2} - w_3\mathbf{z}_{\bar{2}3}) + \frac{2k_l^2}{k_l + k_s} \left[-2\sqrt{3}(-\frac{w_1}{3} + \frac{2w_2}{3} - \frac{w_3}{3})\mathbf{z}_{\bar{3}\bar{2}} + 2\sqrt{3}(-\frac{w_1}{3} - \frac{w_2}{3} + \frac{2w_3}{3})\mathbf{z}_{\bar{2}\bar{3}} \right] + \frac{4k_lk_s}{k_l + k_s} [(w_1 - w_3)\mathbf{z}_{\bar{2}\bar{3}} + (w_1 - w_2)\mathbf{z}_{\bar{3}\bar{2}}] \right\}, \quad (\text{C.5})$$

$$\mathbf{M}_1 = \frac{a}{A} \left\{ 4\sqrt{3}k_l(w_2\mathbf{z}_{\bar{2}\bar{3}} - w_3\mathbf{z}_{\bar{3}\bar{2}}) + \frac{2k_l^2}{k_l + k_s} \left[2\sqrt{3}(\frac{w_1}{3} - \frac{2w_2}{3} + \frac{w_3}{3})\mathbf{z}_{\bar{2}\bar{3}} - 2\sqrt{3}(\frac{w_1}{3} + \frac{w_2}{3} - \frac{2w_3}{3})\mathbf{z}_{\bar{3}\bar{2}} \right] + \frac{4k_lk_s}{k_l + k_s} [(w_1 - w_3)\mathbf{z}_{\bar{2}\bar{3}} + (w_1 - w_2)\mathbf{z}_{\bar{3}\bar{2}}] \right\}. \quad (\text{C.6})$$

$$\mathbf{A}_1 = \frac{4k_lk_sa^2}{(k_l + k_s)A} [(w_2 - w_1)\mathbf{z}_{\bar{2}} + (w_3 - w_1)\mathbf{z}_{\bar{3}}], \quad (\text{C.7})$$

$$\mathbf{A}_2 = \frac{a}{A} \left\{ \frac{4k_lk_sa}{k_l + k_s} [(w_1 - w_2)\mathbf{z}_{\bar{2}} + (w_1 - w_3)\mathbf{z}_{\bar{3}}] + \frac{2k_lk_s\ell}{k_l + k_s} [(w_1 - w_2)\mathbf{z}_{\bar{2}} + (w_1 - w_3)\mathbf{z}_{\bar{3}}] \right\}, \quad (\text{C.8})$$

$$Q = \frac{1}{A} \left[12k_b + 4k_l(w_1^2 + w_2^2 + w_3^2) - \frac{8k_l^2}{3(k_l + k_s)}(w_1^2 + w_2^2 + w_3^2 - w_1w_2 - w_2w_3 - w_3w_1) \right], \quad (\text{C.9})$$

where $\mathbf{z}_{pqrs} = \mathbf{z}_p \otimes \mathbf{z}_q \otimes \mathbf{z}_r \otimes \mathbf{z}_s$ are tensors. Note that again a superimposed bar symbolizes a plane rotation of $\pi/2$, such as $\mathbf{z}_{\bar{1}\bar{2}} = \bar{\mathbf{z}}_1 \otimes \bar{\mathbf{z}}_2$.

Appendix D. Sample preparation and experimental setup

The experimental samples in Figs. A.3 and A.4 are fabricated by a fiber laser-cutting machine. The Kagome lattices consisting of rigid triangles connected by elastic hinges are made of steel (Young's modulus $E = 209$ GPa, Poisson's ratio $\nu = 0.269$, density $\rho = 7890$ kg/m³). The sample dimensions and main geometrical parameters are the following: length of lattice vector $d = 20$ mm, side length of triangles $L = 10$ mm, thickness $h = 1.5$ mm, fillet radius of hexagonal holes $r = 2$ mm. A reflective mirror spray paint is applied to the samples, enhancing its ability to reflect the bright lights required for short camera exposures.

Fig. A.5 shows the experimental setup. Samples are tested using an MTS Landmark 370 servo-hydraulic system (MTS, Eden Prairie, Minnesota, USA). To produce results comparable to the numerical simulations under static loading, the testing speed is controlled by a constant cross head speed of 0.001 mm/s. In addition, the 3D Digital Image Correlation (DIC) System Q-400 (Dantec Dynamics, Tonsbækken, Skovlunde, Denmark) is used for displacement field measurements.

Appendix E. Numerical simulations

The finite-element method simulations in this work are all performed using the commercial software COMSOL Multiphysics and linear elasticity is used as a material model, with Young's modulus $E = 209$ GPa, Poisson's ratio $\nu = 0.269$, density $\rho = 7890$ kg/m³ in plane stress conditions. Eigenfrequency calculations within the "Solid Mechanics module" are carried out to find the dispersion relations in Figs. 3 and 9, and distribution of zero modes in Fig. 4. Large-scale simulations are then implemented by the "Solid Mechanics module" and stationary calculations are performed to obtain the displacement fields in Figs. 5–8 and A.6.

Appendix F. Additional numerical and experimental results

In this section, we examine elastic responses of the regular beam and the polarized beam I under three-point bending test, as shown in Fig. A.6. Using test machine MTS, these two beams are mounted in a three-point bending configuration and a 50 N loading is applied at the top center of the lattice. Our experimental measurement, numerical simulation and microtwist model demonstrate that there exists a symmetric bending curve in the regular beam (Fig. A.6a) while an asymmetric bending curve in the polarized beam (Fig. A.6b). By comparing Fig. 7b, Fig. A.6a and Fig. A.6b, it should be interesting to mention that the degree of symmetry is significantly increased with the increase of the distortion parameters. We further plot the vertical displacement field of the regular beam (resp. polarized beam I) by extracting from the numerical simulation in Fig. A.6b (resp. Fig. A.6f), the DIC measurement in Fig. A.6c (resp. Fig. A.6g) and the microtwist model in Fig. A.6d (resp. Fig. A.6h). These three plots have good agreement and further validate the microtwist elasticity theory.

Appendix G. Cauchy continuum

Consider a periodic lattice undergoing a uniform macroscopic strain \mathbf{E} , with respect to the Cauchy–Born hypothesis (Born et al., 1955; Hutchinson and Fleck, 2006; Phani and Hussein, 2017), the displacement field is the summation of two parts: the linear deformation obtained by a macroscopic strain and the periodic displacement field of each unit cell. Accordingly, the displacement filed is expressed as:

$$\mathbf{u}_i^{m,n} = \mathbf{E} \cdot \mathbf{x}_k^{m,n} + \Delta \mathbf{u}_i^{m,n}. \quad (\text{G.1})$$

Here, the rotation gradients are ignored, $\nabla\varphi = \mathbf{0}$, and the extra stress $s = 0$. Then, our microtwist continuum reduces to the Cauchy continuum, where the twisting motion φ is given by

$$\varphi = -\frac{\mathbf{M}_1 : \nabla^s \mathbf{U}}{Q}, \quad Q \neq 0, \quad (\text{G.2})$$

and the constitutive relationship is recast into the form

$$\sigma = \mathbf{C}^* : \nabla^s \mathbf{U}, \quad \mathbf{C}^* = \mathbf{C} - \frac{1}{Q} \mathbf{M} \otimes \mathbf{M}_1. \quad (\text{G.3})$$

By comparing Eqs. (55) and (G.3), it is seen that the Cauchy–Born hypothesis greatly simplifies the constitutive law. However, it dismisses the possibility of there being any coupling between the macroscopic strain and the rotation gradient. Taking this coupling into account will significantly improve the quality of the predictions of the effective medium theory; quantitative demonstrations are presented in Section 5.1.

References

Bilal, O.R., Süssstrunk, R., Daraio, C., Huber, S.D., 2017. Intrinsically polar elastic metamaterials. *Adv. Mater.* 29, 1700540.

- Born, M., Huang, K., Lax, M., 1955. Dynamical theory of crystal lattices. *Amer. J. Phys.* 23, 474.
- Chen, Y., Wu, B., Li, J., Rudykh, S., Chen, W., 2021. Low-frequency tunable topological interface states in soft phononic crystal cylinders. *Int. J. Mech. Sci.* 191, 106098.
- Cosserat, E., Cosserat, F., 1909. *Theorie des corps déformables*. A. Hermann et fils.
- Coulais, C., 2016. Periodic cellular materials with nonlinear elastic homogenized stress-strain response at small strains. *Int. J. Solids Struct.* 97–98, 226–238.
- Coulais, C., Sabbadini, A., Vink, F., van Hecke, M., 2018. Multi-step self-guided pathways for shape-changing metamaterials. *Nature* 561, 512–515.
- Czajkowski, M., Coulais, C., van Hecke, M., Rocklin, D.Z., 2022. Conformal elasticity of mechanism-based metamaterials. *Nat. Commun.* 13 (211).
- Day, A., Snyder, K., Garboczi, E., Thorpe, M., 1992. The elastic moduli of a sheet containing circular holes. *J. Mech. Phys. Solids* 40, 1031–1051.
- Grima, J.N., Evans, K.E., 2000. Auxetic behavior from rotating squares.
- Hutchinson, R.G., Fleck, N.A., 2006. The structural performance of the periodic truss. *J. Mech. Phys. Solids* 54, 756–782.
- Kadic, M., Bückmann, T., Stenger, N., Thiel, M., Wegener, M., 2012. On the practicability of pentamode mechanical metamaterials. *Appl. Phys. Lett.* 100, 191901.
- Kane, C.L., Lubensky, T.C., 2014. Topological boundary modes in isostatic lattices. *Nat. Phys.* 10, 39–45.
- Li, X., Chen, Y., Zhu, R., Huang, G., 2021. An active meta-layer for optimal flexural wave absorption and cloaking. *Mech. Syst. Signal Process.* 149, 107324.
- Liang, X., Crosby, A.J., 2020. Programming impulsive deformation with mechanical metamaterials. *Phys. Rev. Lett.* 125, 108002.
- Ma, G., Xiao, M., Chan, C.T., 2019. Topological phases in acoustic and mechanical systems. *Nat. Rev. Phys.* 1, 281–294.
- Milton, G.W., 2013. Complete characterization of the macroscopic deformations of periodic unimode metamaterials of rigid bars and pivots. *J. Mech. Phys. Solids* 61, 1543–1560.
- Milton, G.W., Cherkaev, A.V., 1995. Which elasticity tensors are realizable? *J. Eng. Mater. Technol.* 117 (483).
- Nassar, H., Chen, Y., Huang, G., 2018. A degenerate polar lattice for cloaking in full two-dimensional elastodynamics and statics. *Proc. R. Soc. A* 474, 20180523.
- Nassar, H., Chen, Y., Huang, G., 2019. Isotropic polar solids for conformal transformation elasticity and cloaking. *J. Mech. Phys. Solids* 129, 229–243.
- Nassar, H., Chen, H., Huang, G., 2020a. Microtwist elasticity: A continuum approach to zero modes and topological polarization in kagome lattices. *J. Mech. Phys. Solids* 144, 104107.
- Nassar, H., Chen, Y., Huang, G., 2020b. Polar metamaterials: a new outlook on resonance for cloaking applications. *Phys. Rev. Lett.* 124, 084301.
- Norris, A.N., Shuvalov, A.L., 2011. Elastic cloaking theory. *Wave Motion* 48, 525–538.
- Phani, A.S., Hussein, M.I., 2017. *Dynamics of Lattice Materials*. John Wiley & Sons.
- Rocklin, D.Z., Zhou, S., Sun, K., Mao, X., 2017. Transformable topological mechanical metamaterials. *Nature Commun.* 8, 1–9.
- Xia, R., Nassar, H., Chen, H., Li, Z., Huang, G., 2021. Microtwist homogenization of three-dimensional pyrochlore lattices on zero modes and mechanical polarization. *J. Mech. Phys. Solids* 155, 104564.
- Xu, X., Wang, C., Shou, W., Du, Z., Chen, Y., Li, B., Matusik, W., Hussein, N., Huang, G., 2020. Physical realization of elastic cloaking with a polar material. *Phys. Rev. Lett.* 124, 114301.
- Zhang, H., Chen, Y., Liu, X., Hu, G., 2020. An asymmetric elastic metamaterial model for elastic wave cloaking. *J. Mech. Phys. Solids* 135, 103796.
- Zhou, W., Wu, B., Chen, Z., Chen, W., Lim, C., Reddy, J., 2020. Actively controllable topological phase transition in homogeneous piezoelectric rod system. *J. Mech. Phys. Solids* 137, 103824.